

Wireless Power Monitoring at Plugs and Panels

Michael Lorek



Electrical Engineering and Computer Sciences
University of California at Berkeley

Technical Report No. UCB/EECS-2017-176

<http://www2.eecs.berkeley.edu/Pubs/TechRpts/2017/EECS-2017-176.html>

December 1, 2017

Copyright © 2017, by the author(s).
All rights reserved.

Permission to make digital or hard copies of all or part of this work for personal or classroom use is granted without fee provided that copies are not made or distributed for profit or commercial advantage and that copies bear this notice and the full citation on the first page. To copy otherwise, to republish, to post on servers or to redistribute to lists, requires prior specific permission.

Wireless Power Monitoring at Plugs and Panels

by

Michael Christian Lorek

A dissertation submitted in partial satisfaction of the

requirements for the degree of

Doctor of Philosophy

in

Engineering – Electrical Engineering and Computer Sciences

in the

Graduate Division

of the

University of California, Berkeley

Committee in charge:

Professor Kristofer S.J. Pister, Chair
Associate Professor Michel M. Maharbiz
Professor Paul Wright

Fall 2015

The dissertation of Michael Christian Lorek, titled Wireless Power Monitoring at Plugs and Panels, is approved:

Chair	_____	Date	_____
	_____	Date	_____
	_____	Date	_____

University of California, Berkeley

Wireless Power Monitoring at Plugs and Panels

Copyright 2015
by
Michael Christian Lorek

Abstract

Wireless Power Monitoring at Plugs and Panels

by

Michael Christian Lorek

Doctor of Philosophy in Engineering – Electrical Engineering and Computer Sciences

University of California, Berkeley

Professor Kristofer S.J. Pister, Chair

In 2012, electricity generation was responsible for over 30% of carbon emissions in the US - surpassing the transportation sector - and predictions to 2040 show this trend continuing with current technologies. Electrical submetering provides improved spatial and temporal resolution into how buildings use their energy, and case studies have shown that improvements driven by submetering data can lead to 5-30% reductions in electrical energy usage. However, traditional building submetering technologies present unfavorable cost, installation, and form factor attributes that inhibit the widespread deployment of these systems. This dissertation details the design and characterization of easy-to-install, low-cost wireless sensors for submetering building electrical power at the circuit breaker and plug load levels.

Discussed first is a sensor installed on the external face of a circuit breaker that non-intrusively measures line voltage and circuit current waveforms, and calculates the real power dissipated in that circuit. The PCB-based sensor uses a Hall effect sensor, a 1920 Hz sampling rate to handle non-linear loads, can measure power levels below 10W, uses all off-the-shelf components with a BOM under \$10, and can be installed without hiring an electrician. The total installed cost to submeter an entire panel using the sensor system is roughly \$250 - a 10x reduction compared to traditional technologies. Data is presented that verifies the efficacy of the submetering sensor system in a lab setting as well as a real-world residential installation.

Next, the details of a plug-through energy monitor for ubiquitous electrical monitoring of plug load devices in buildings is presented. Using a non-invasive inductive current sensing technique, the current flowing through a plug load device is measured without a series-sensing element that breaks the circuit. This enables slim profile hardware, and eliminates the series resistor power dissipation inherent in traditional current sensing implementations. The prototype can be embedded into an outlet faceplate and easily retrofit onto any existing outlet for long-term measurement of AC power parameters. The sensor includes 802.15.4 wireless connectivity, a 1920 Hz sampling rate, and a measured noise floor of approximately 2W with a BOM around \$5.

The new sensor technologies presented in this dissertation are shown to be effective power meters, and are also cheap to build with standard printed circuit board manufacturing processes. Thus, these meters are commercially viable and have the potential to bring building submetering to the masses. Commercial building owners could save over \$0.20/ft²-yr by spending approximately \$0.15/ft² to install plug and panel metering. Given an average household, homeowners could save over \$130/yr with a \approx \$375 investment to meter their panel and wall outlets. If this technology was installed in all US residential and commercial buildings, the reduction of greenhouse gas emissions would be equivalent to that of over 2 *trillion* miles driven every year in a 30 mpg car. In buildings that are very inefficient, a much greater reduction in consumption is possible. With continued development and integration, ideas presented in this work could lower the cost of the metering hardware by another 5-10x, and make the goal of ubiquitous electricity submetering more easily attainable.

To Alice.

Contents

Contents	ii
List of Figures	iv
List of Tables	vi
1 Introduction	1
2 Electricity Metering Background	4
2.1 Overview	4
2.2 Metering Hardware State-of-the-Art	5
2.3 Buildings Research Case Studies	8
3 Peel-and-Stick Electricity Meter for Panel Submetering	11
3.1 Introduction	11
3.2 System Overview	13
3.3 Sensing Implementation	15
3.4 Experimental Results	16
3.5 Comparison to State-of-the-Art	26
4 Plug-Through Energy Monitor for Wall Outlet Electrical Devices	27
4.1 Introduction	27
4.2 Inductive Current Sensing	27
4.3 Sensor System Design	30
4.4 Experimental Results	35
4.5 Comparison to State-of-the-Art	39
5 Future Work	43
5.1 Tunneling Magnetoresistive Sensor for PASEM	43
5.2 Single-Chip Vector Sensing Breaker Meter	45
6 Conclusions	47

Bibliography

List of Figures

1.1	2013 US greenhouse gas emissions [1].	1
1.2	US residential electricity usage predicted to 2040 [2].	2
1.3	US commercial electricity usage predicted to 2040 [2].	3
2.1	(a) Traditional current-transformer-based in-panel submeter installation. (b) Wiring diagram showing voltage and current measurement signal lines.	6
2.2	(a) Kill A Watt EZ plug load meter [21]. (b) SmartPower Outlet plug load meter [22]. Image credits: [23], [24].	8
3.1	PASEM system block diagram showing sensing techniques, PASEM, and wireless base station.	11
3.2	PASEM system installation on circuit breaker panel. Five PASEM devices installed with wireless base station at bottom. Circuit breakers labeled for reference.	12
3.3	Assembled Peel-and-Stick Electricity Meter with US quarter dollar coin for size reference.	13
3.4	Signal processing block diagram showing current and voltage analog sensing circuits, and DSP real power calculation technique.	14
3.5	(a) Thermal-actuated circuit breaker innards with bimetallic strip and PASEM placement annotated. (b) Magnetic-actuated circuit breaker innards with solenoid and PASEM placement annotated.	17
3.6	PASEM output vs. reference power meter, showing great correlation to sub-10W load powers.	18
3.7	Long-term, 480V 3-phase line-neutral voltage measurement. PASEM analog V_{sense} output vs. contact-based measurement.	19
3.8	Measured current-voltage phase difference for a resistive load.	20
3.9	Real power calculation error vs. power factor for various phase errors. Real-world loads are typically designed to have $PF > 0.9$	21
3.10	(a) Sampled I_{sense} , V_{sense} , and phase-corrected line voltage signals for a TRIAC dimmer with resistive load. (b) FFT of sampled I_{sense} signal in (a).	22
3.11	PASEM residential kitchen circuit vs. whole house meter data.	23
3.12	Circuit breaker panel crosstalk vector illustration.	24
3.13	Real power measured by all five sensors due to a load on the center circuit.	25

4.1	(a) PTEM sensor PCB. (b) PTEM installed on outlet with 3D-printed faceplate. (c) Kill A Watt EZ plugged into installed PTEM for size comparison.	28
4.2	Inductive current sensing conceptual diagram.	29
4.3	Magnetic flux density vector field plot around plug conductors and sense coil region. Model assumes infinite wire currents with locations annotated.	31
4.4	Spatial variation of B_y between plug conductors, per Amp through the load. Model assumes infinite wire currents with locations annotated.	32
4.5	AC-DC converting power supply circuit.	32
4.6	Inductive current sensing analog front end.	33
4.7	Line voltage sensing analog front end.	34
4.8	PTEM i_{sense_1} vs. current transformer for various i_{load_1} , with $i_{load_2} = 0$	36
4.9	TRIAC dimmer with resistive load; top: $v_{sense}(t)$, middle: $i_{load_1}(t)$, bottom: FFT[$i_{load_1}(t)$].	38
4.10	Entertainment center power timeseries with ≈ 30 second smoothing. Digital cable box, cable modem, and wireless router always on.	39
4.11	i_{load_1} and i_{load_2} signals. No crosstalk cancellation algorithm.	40
4.12	Deconvolved i_{load_1} and i_{load_2} signals. Crosstalk cancellation algorithm active.	41
5.1	TMR sensor measured frequency response.	44
5.2	(a) Single-chip vector magnetic field sensing power meter block diagram. (b) PCB prototype sensor with 4x4x2 array of 3-axis magnetic field sensors.	45
5.3	Measured magnetic field with 4x4x2 vector sensor array on solenoidal circuit breaker.	46

List of Tables

3.1	Simplified bill of materials for PASEM board.	14
3.2	PASEM sensor comparison to state-of-the-art.	26
4.1	PTEM sensor comparison to state-of-the-art.	42
5.1	PASEM Hall effect sensor vs. TMR sensor comparison table.	43

Acknowledgments

Professor Pister - thank you for welcoming me into your research group when I was an orphan in my first year, and for providing me with the opportunity to work on a plethora of very exciting research projects. I really appreciate you always finding a way for me to be funded for my work. Your intuition and knowledge of systems in so many different energy domains is astonishing and something I strive to develop. It is very inspiring to see your mind at work on many difficult problems..."how hard could it be?" Thank you for all of your valuable technical, professional, and life advice over the last six years, and for being very accommodating to circumstances in my life outside of graduate school.

Steven Lanzisera - thank you for teaching me a lot about designing sensing circuits and systems that can be realistically deployed in the real world. Thanks for all of your good advice in regards to navigating grad school. I really enjoyed working together.

Professor Maharbiz - Cyborg flies... those were exciting times! Thanks for all the research advice, funding help in my early years, and laughs. Cornholio.

Mom - thank you for cracking the whip and keeping me focused on my schoolwork when I was young. Thank you for always believing in me and believing that I can accomplish anything. Thank you for never holding me back, and helping me chase my dreams.

Dad - thank you for molding my engineering mindset, starting from when I was a young child. Thank you for fostering my fascination with computers during the golden years of PC gaming. Great times. I wouldn't be where I am today if it wasn't for all the things you have taught me and done for me!

Betsy - thank you for always being there for me. Thank you for giving me a lot of great life advice, and for providing me an outlet when I need it. We have had many great times over the last 28 years and will have many more! Apologies for kicking you in the shins when I was young.

Grandpa - thank you for all the wise advice you have given me throughout my life. I am a much better person because of it. Thank you for your generous contributions towards my education. I'll be thinking of you when I'm hoisting one.

Daisy - thank you for sticking by my side through good and bad times. You do so many nice things for me; I am forever indebted to you. Thank you for always believing in me. You are my better half.

Big thanks to all of the Pister group members that I have had the pleasure to be around. Thank you for all of the enjoyable times in and out of school. Special thanks to Fabien for all your hard work and late nights on the power sensing work - it was fun! Thanks to David Burnett for your work on the energy harvester chip design. Travis, thanks for being a great neighbor. I enjoyed all of our discussions when we were on the late-night grind together. I also had a great time working on the cyborg fly project with you. Thanks to Jessica Iwamoto for your hard work and valuable contributions during summer 2014.

Thanks to the following people for the productive in-depth technical discussions relating to my work: David Burnett, Steven Callender, Fabien Chraim, Daniel Contreras, Daniel

Drew, Igor Izyumin, Mitchell Kline, Filip Maksimovic, Travis Massey, Pramod Murali, Richie Przybyla, Siva Thyagarajan, and Xavier Vilajosana.

EECS, BSAC, and SWARM staff - Thanks for all of your hard work... the research gears wouldn't grind as hard without you!

To the following people I have befriended during my tenure at Berkeley: thank you for all the fun times doing non-engineering things. We sure have had some great ones. I look forward to more fun times together in the future. In rough chronological order: Katerina Papadopoulou, Steven Callender, Henry Barrow, Bobby Schneider, Michael Eggleston, Andrew Mairena, Brian Pepin, Will Biederman, Dan Yeager, Milos Jorgovanovic, Richie Przybyla, Fabien Chraim, Jared Friedman, Andrew Melvin, and Adrian Avendano.

Thanks to the other great friends in my life that have been by my side during this journey: Bennet Krawchuk, Sean Danko, Dan Brown, Jeff Dardis, Joe Lippitt, Trevor Holloway, and Jon Miller.

Chapter 1

Introduction

Electricity generation has been the dominant source of greenhouse gas (GHG) emissions in the United States for many years, based on estimates dating back to 1990 [1]. In the US in 2013, approximately 2,100 million metric tons of CO₂ equivalent were created by the generation of approximately 3.8 trillion kWh of electricity [2]. Around 39% of this electrical energy was generated from coal, 27% from natural gas, and 13% from renewable resources. As seen in Figure 1.1, electricity generation was responsible for 31% of all US GHG emissions in 2013, compared to 27% attributed to the transportation sector. Upon further dissection of the 2013 US GHG emissions due to electricity generation, it is shown that approximately 36% were created by electricity usage in the residential sector, and 35% from the commercial sector. Thus, the electricity used in buildings that we interact with on a daily basis is making a substantial negative impact on the environment due to the associated greenhouse gas emissions.

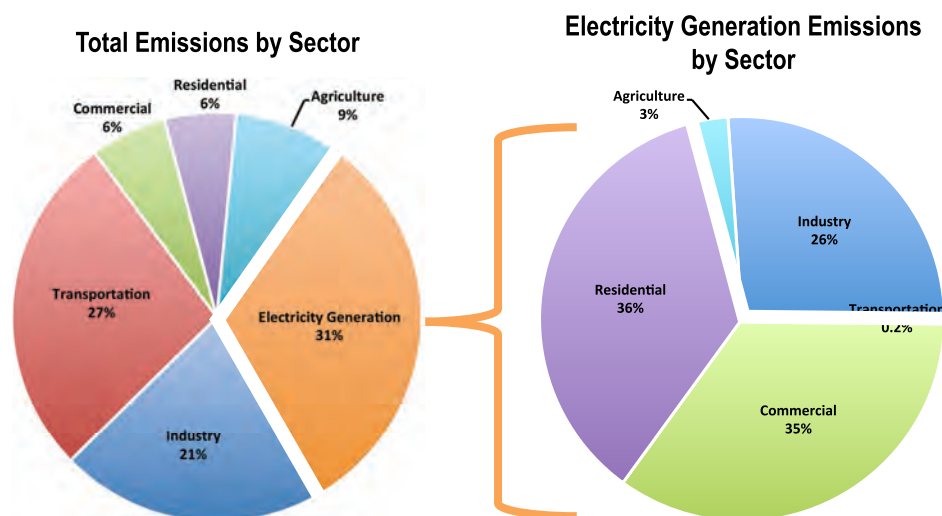


Figure 1.1: 2013 US greenhouse gas emissions [1].

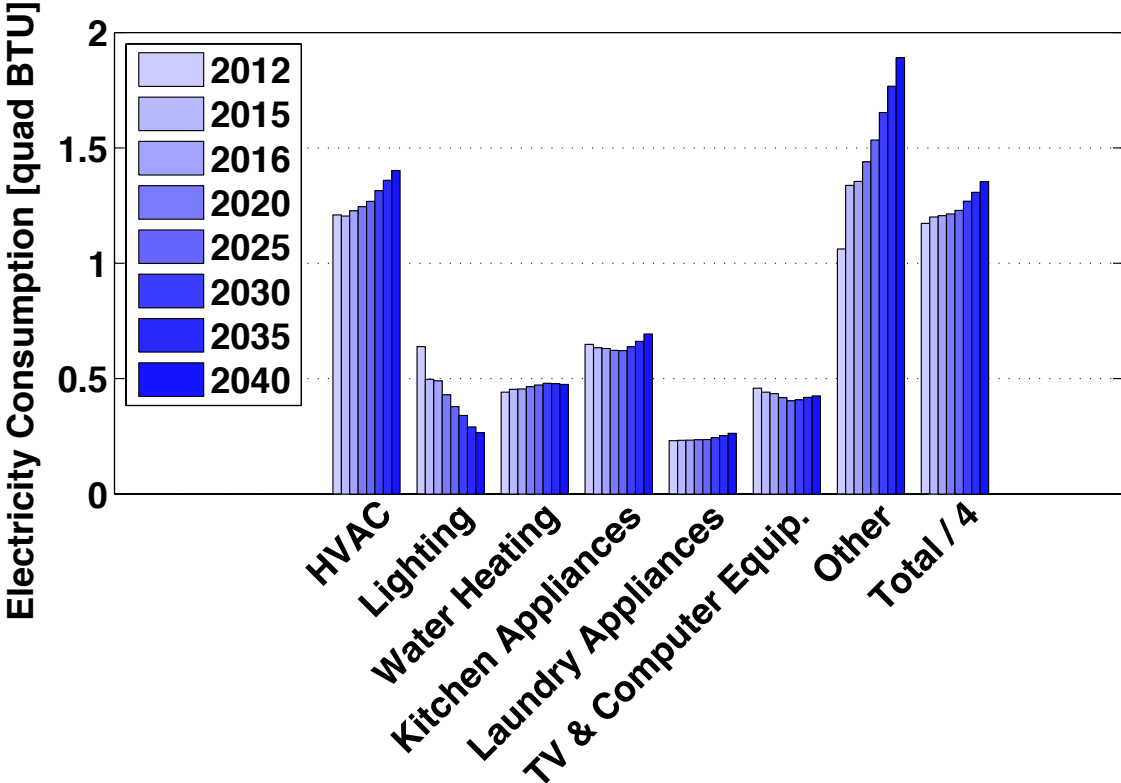


Figure 1.2: US residential electricity usage predicted to 2040 [2].

The breakdown of electrical energy dissipation by end use in US residential and commercial buildings with projections to 2040 can be seen in Figures 1.2 and 1.3, respectively [2]. While core building requirements such as heating, ventilation, air conditioning (HVAC), and lighting were previously the major electrical energy sinks in buildings, that is no longer the case today. In 2015, Figures 1.2 and 1.3 show that the electricity consumption attributed to the 'Other' category - miscellaneous plug loads that are not required for typical building functioning and occupancy - is the dominant end use in both building types of discussion. Therefore, plug load devices need to be a major focus in efforts to reduce the greenhouse gas emissions caused by electricity usage in buildings.

Projections to 2040¹ do not show a reduction in building electrical energy usage or GHG emissions based on the development and adoption of current technologies [2]. These estimates also show plug loads' electricity usage to increase exponentially and become an increasingly problematic electrical energy sink in buildings. The portion of electricity generated from coal in 2040 is predicted to decrease slightly to from 39% to 34% due to greater use of clean energy sources, however, overall GHG emissions still increase due to higher total electricity generation. Therefore, it is critical for new solutions to be developed and deployed that

¹Based on Reference case projection: a "business-as-usual trend estimate, given known technology and technological and demographic trends."

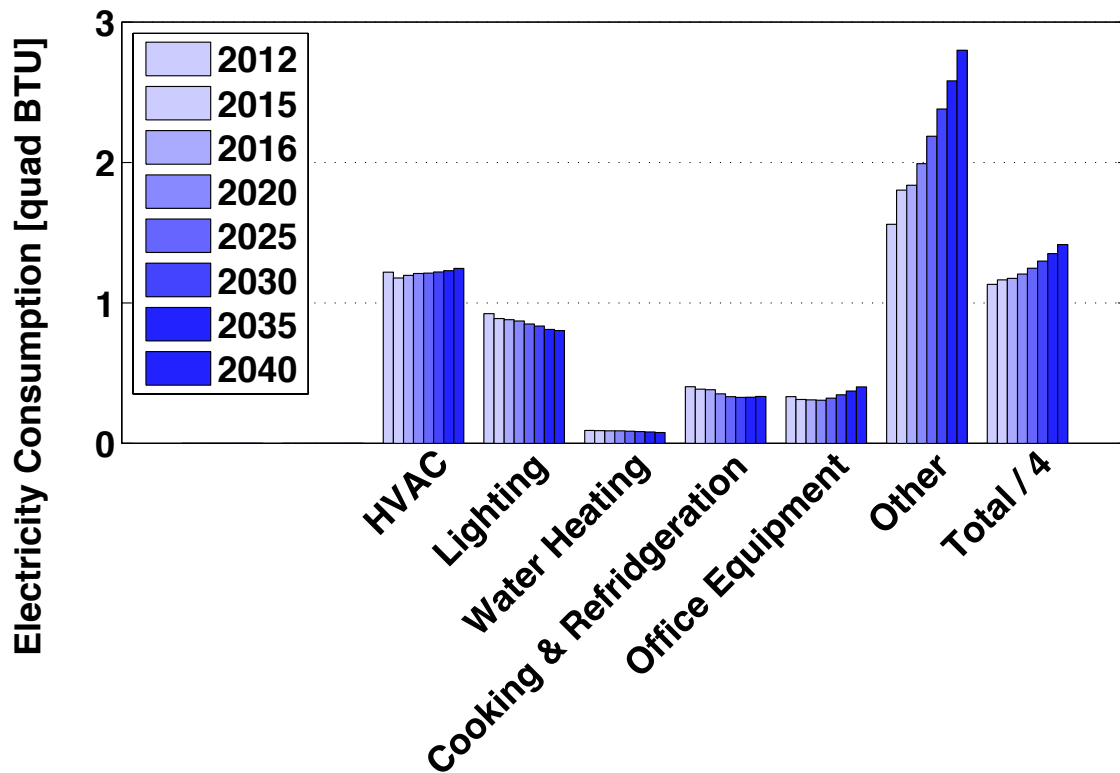


Figure 1.3: US commercial electricity usage predicted to 2040 [2].

reduce greenhouse gas emissions by making buildings more energy efficient, in addition to the continued proliferation of renewable energy sources. In this work, novel sensor technologies for wireless electrical submetering at circuit breaker panels and plug loads is presented as a practical and effective way to reduce electricity usage in buildings.

Chapter 2

Electricity Metering Background

2.1 Overview

In the last fifteen years, intelligent whole-building electricity meters have been deployed in a handful of states, including the PG&E SmartMeter [3] in California. These devices provide two-way communication between the electricity provider and each metered building. This enables the utility provider to charge rates that vary across the day and reward customers for using electricity during periods of lower demand on the electrical grid. A customer can also visualize a time series of their building's aggregate electricity usage in an online interface to help them be more energy conscious. Building electrical submetering aims to meter the electricity usage in buildings at the circuit and/or plug levels to obtain electricity usage information with higher spatial and temporal resolution.

Submetering generates data that is more disaggregated to end use and ideally measures the electricity usage of individual loads directly. Compared to whole-building electricity data, submetering data is more valuable to building managers and tenants. The data provides detailed insight into how a building's electrical energy is dissipated, and is fed into a central smart building management system for logging, visualization, and algorithmic processing. With metering points closer to the end electrical loads, sensor data better highlights faulty or outdated building electrical appliances and enables monitoring-based commissioning to improve energy efficiency. Monitoring-based commissioning is the process of continuously examining a building's metering data to identify beneficial retrofits, verify energy efficiency improvements after retrofits, and track the building's performance over time. Submetering data also more effectively motivates tenants to change their behavior in order to save energy, since the data is more closely associated with their habits and actions in the building.

Buildings research shows that electricity submetering combined with data analytics and maintenance follow-up can reduce buildings' electricity usage by 5% to 30%, across a wide range of building types [4]–[11]. However, very few buildings are outfitted with the submeters required to achieve these savings because of various factors, including: expensive hardware and installation costs, lengthy installation times, and intrusive metering hardware. For me-

tering at the circuit breaker panel, the installed cost of current technologies is typically over \$1,000 per panel, and plug load metering costs around \$50 per outlet with wireless communication. In order to promote the widespread deployment of building electrical submetering and realize the associated impactful environmental benefits, it is critical to develop new sensor technologies that are unobtrusive, easy to install, and cheap.

2.2 Metering Hardware State-of-the-Art

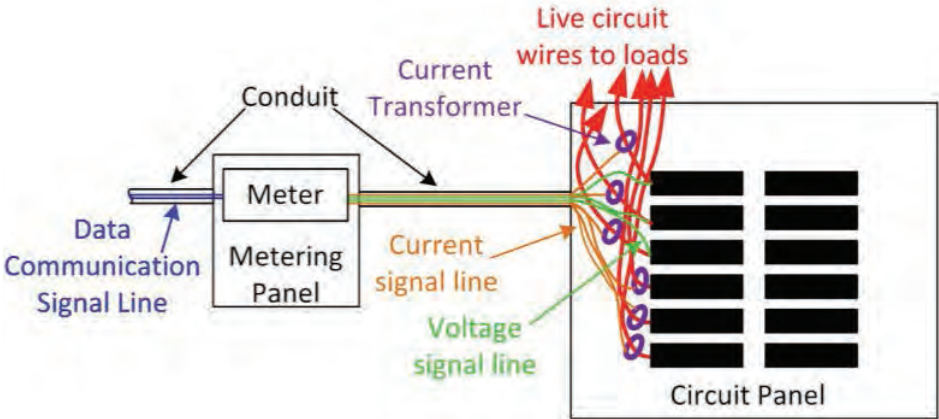
Circuit Breaker Panel Meters

Today’s commercially available circuit breaker panel submetering technologies require bulky current transformers (CTs) and voltage connections to be installed inside the panel. A photo of a traditional submetering installation is shown in Figure 2.1a, and a wiring diagram of the system in Figure 2.1b. To install a system such as this, an electrician must either shut down the building’s power or perform dangerous hot work on the panel. The installer must remove the electrical panel’s protective cover, and spend significant time to install metering components, external conduit, and enclosures to cover the equipment and signal leads. The total installation cost can subsequently be dominated by the labor required to carefully install all hardware, conduit, and wiring by skilled tradespeople, while also adhering to safety and building code requirements. This results in an installed cost that is approximately \$1,000 – \$5,000 per panel [5], [12], [13]. Thus, a typical mid-size, mid-life commercial building requiring several tens of metered panels can cost up to \$100,000 for three-phase submetering. The time required to recoup the costs associated with the submetering installation are then undesirably long, and building owners are less likely to make the investment. Therefore, a great need exists for a circuit breaker panel submetering system that can be installed without an electrician for minimal time and money expenditure.

To meet these goals, it was proposed to replace the in-panel hardware with wireless, non-contact-based sensor devices placed on the outside of the circuit breakers. This provides a number of benefits. First, installation on the outside of the circuit breaker panel does not require an electrician. Second, since the system is self-contained on the exterior panel face, no external wiring or conduit must be installed. The idea of fastening a sensor to the external face of a circuit breaker to non-intrusively measure the circuit’s current was first published in 2010, by researchers at UC Berkeley [14]. In this work, the authors designed a mesoscale (≈ 4 cm long) piezoelectric cantilever with permanent magnets at its tip. In a magnetic field, the cantilever deflects and a voltage can be measured that is proportional to the incident field, and, subsequently, the nearby electric current. These cantilever-based current sensors were shown to be linear and have a current measurement noise floor of approximately $0.17 A_{RMS}$ when installed on a circuit breaker. No external power supply is fundamentally required for these devices, and the sensor actually extracts energy from the external magnetic field that could be used to power the rest of the sensor node’s electronics. The cm-scale devices are capable of extracting $22\mu W$ of power with $12 A_{RMS}$ flowing through a circuit breaker at 60



(a)



(b)

Figure 2.1: (a) Traditional current-transformer-based in-panel submeter installation. (b) Wiring diagram showing voltage and current measurement signal lines.

Hz, and a 1 M Ω load connected across the cantilever. Later work integrated the mesoscale sensors with interface electronics and an 802.15.4 wireless link, providing proof of concept that non-intrusive current measurement at the circuit breaker face could be used to track real-world loads [15].

Another non-intrusive sensor designed for the face of circuit breakers was presented in 2013 [16]. This work used a giant magnetoresistive (GMR) magnetic field sensor to measure a circuit breaker's current. The sensor node is an assembly of three printed circuit boards (PCBs), including a Zigbee radio and a rechargeable battery. It occupies a volume of 0.56 cm³, and is claimed to be the smallest Zigbee-compatible sensor node in existence at the time of publication. While very impressive from a size standpoint, the system suffers from signal integrity issues including non-linearity and hysteresis, in addition to having short battery life, which limit its real-world metering applicability.

While non-contact-based panel meters have previously been presented in the literature, they suffer from multiple drawbacks that make widespread deployment difficult and limit the practical value of the data that is acquired. Multiple works have shown current magnitude sensors, but these systems do not sense the line voltage, and, thus, cannot calculate real power dissipation [14]–[17]. Many of these systems also have low sampling rates that do not perform well with non-linear loads, and prevent the ability to detect and diagnose load faults by examining the spectral content of the acquired signals. In [18], a 1 kHz current signal sample rate is reported, however the sensor itself is too large to submeter individual circuit breakers, and the system has difficulty dealing with multi-phase power systems. The new sensor system detailed in Chapter 3 of this dissertation solves all of these problems and offers a low-cost, practical, and effective circuit submetering solution [19], [20].

Plug Load Meters

Various plug load meters exist commercially today, many of which are sold at common brick and mortar stores such as Home Depot and Lowe's. These meters typically sell for around \$50 with and \$20-30 without wireless connectivity; examples of these meters are shown in Figure 2.2. Today's meters are expensive, sit visibly at the wall outlet, are physically and aesthetically obtrusive, and often block neighboring duplex receptacles. As a result of these drawbacks, the meters are mainly used for occasional auditing of devices' energy usage as opposed to widespread continuous monitoring.

One plug load sensor proposed in the literature is tied to a plug load's power cable, and calculates the load current by monitoring the magnetic field [25]. This sensor is small and non-intrusive, however it requires a unique calibration profile for every load. The calibration is automatic, but requires a circuit breaker panel meter and a complex algorithm. Computing the calibration for the sensors becomes more intensive as the number of loads grows, and also when the loads' power dissipation and power factor vary with time. Therefore, this solution would be difficult to scale up to large buildings with hundreds of plug loads per panel.

Another plug load sensor developed at the University of Michigan uses a surface mount inductor to measure the current non-intrusively by sensing the associated magnetic field

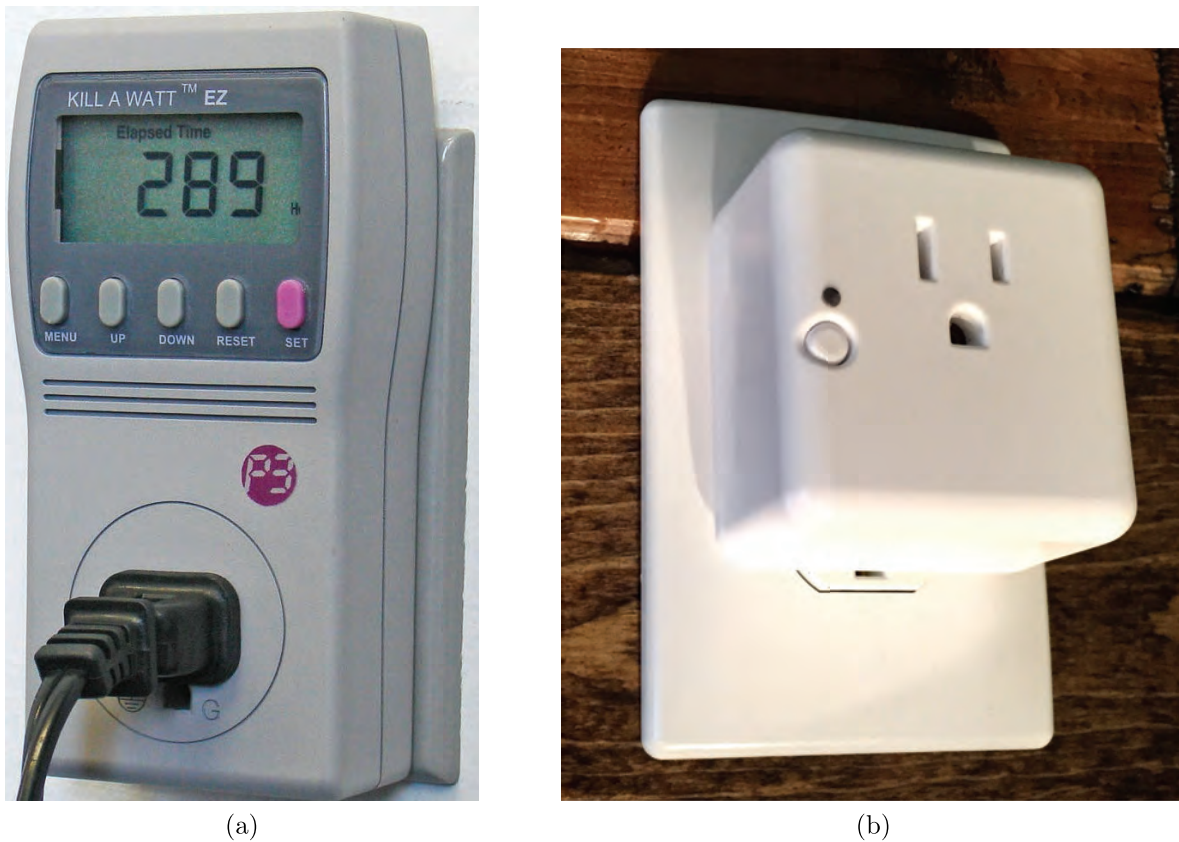


Figure 2.2: (a) Kill A Watt EZ plug load meter [21]. (b) SmartPower Outlet plug load meter [22]. Image credits: [23], [24].

[26]. The sensor is a a slim form factor, and sits between a plug and outlet in a plug-through arrangement. The sensor also measures the line voltage, calculates real power, and transmits data over a Bluetooth Low Energy (BLE) wireless link. The work is similar in a number of ways to the research presented here in Chapter 4 [27], and was published simultaneously. The sensor in [26] will be discussed further in Section 4.5 of this document, after the relevant work in this dissertation has been introduced.

2.3 Buildings Research Case Studies

Commercial

Circuit Metering

The Bank of America building in San Francisco is the second tallest building in the city at 52 stories, with a floor area of 1.5 million square feet [28]. When energy managers realized the building exceeded its energy budget by a factor of three, they took action and installed

120 electrical submeters across half of the building [4]. Even with expensive traditional submetering technologies, the submetering data led to energy savings that paid for the metering installation in a matter of only days. The data enabled improvements that reduced the building's energy consumption by 30%, and saved \$1 million in energy costs in the first year.

Another study was completed at a major tenant residing in a 400,000 ft² commercial space in New York City [4]. After installing electricity submeters and using the data to examine hourly consumption profiles, improvements were identified that reduced the building's total electrical energy consumption by 795,850 kWh, or 18%, in the first year. The peak demand was also decreased by 57 kW, or 8%, due to changes made based on the submetering data. These reductions led to savings of \$160,000 in electric utility costs in one year.

A third study of interest involved three multi-tenant office buildings in Washington, D.C [5]. The results of this study are particularly compelling because the buildings were performing well, with high energy star ratings (71-86) and building management systems before the submetering systems were installed. Even in this case, the submetering data led to 13% lower electricity consumption after one year, averaged over all three buildings. The submetering data highlighted bugs in the pre-existing building management systems that would have otherwise been difficult to track. Energy savings were realized mainly by operational adjustments of control systems, and didn't require any major capital. The first year monetary savings exceeded the submetering installation expenses by \$74,000. These results are very exciting because they show that even buildings with much attention and technology dedicated to maximizing energy efficiency can still see significant improvements from submetering data.

Plug Load Metering

Due to the limitations in plug metering hardware discussed earlier, there is a scarcity of case studies investigating the impact of plug load metering on building energy efficiency. One case study found a 6% reduction in energy was possible by metering workstations in a commercial building and introducing competition between tenants. However, this study left many plug loads unmetered and was conducted in an EPA office building where tenants were likely already energy conscious [6].

Residential

Residential buildings research has thus far focused on improving efficiency using electrical energy data from entire homes and apartments, instead of individual circuits or devices, due to the large expenses associated with the installation of today's submetering systems. An overview of the results of these residential metering studies are discussed below.

Much research was conducted over the last few decades to investigate the impact of displaying energy data in households via an in-home display [4], [7]–[9]. The studies show that feedback of energy information in real-time motivates tenants to change their behaviors,

and can lead to energy reductions of 5-20%. Also promising are research results that show the homes' energy efficiency improvements tend to persist over time [7]. Follow-up interviews with tenants reveal that the energy-saving behavioral changes they made during the study period were no longer actively on their mind, and were integrated into their daily routines and habits.

The New York State Energy Research and Development Authority (NYSERDA) has been performing studies on the impact of individually metering apartments in multi-family buildings for over twenty years [10]. This enables each apartment to be billed independently for only the electricity they use, and, thus, motivates tenants to reduce their energy usage. The results of the NYSERDA case studies indicate that metering each apartment typically reduces the building's energy consumption by 10-26% after the first year. NYSERDA research also shows that these savings tend to persist over long periods of time. Due to the energy improvements they have witnessed first-hand, NYSERDA currently provides incentives for multi-family building owners to install separate meters. As of December 2015, NYSERDA will subsidize 50% of the installed cost, up to \$250 per meter [29].

The addition of circuit or plug submetering systems to these buildings can provide continuous real-time energy information that is much more valuable since it is more disaggregated to the end use of the electricity. It is not a stretch to think that the real-world benefits of submetering in the residential sector would mirror that of the commercial sector, and may even surpass it. Residential tenants have one critical additional incentive compared to the commercial sector: reducing the money paid out of their own pocket every month to the utility provider.

University

A study published in 2009 looked at the impact of monitoring-based commissioning in 26 University of California and California State University campus buildings [11]. Whole-building meters and submeters were installed in the studied buildings and connected to energy information systems. Based on the analyzed meter data, 1120 deficiencies were identified across the buildings; HVAC deficiencies were most common, found at 65% of sites in the study, with air-handling and distribution system deficiencies found at 59% of the locations. Consequently, the most common fixes were adjusting HVAC set points. Without any capital retrofits, the buildings on average reduced their electricity consumption by 9%, and decreased their peak demand by 4%. The study also found that buildings with laboratory facilities saw the greatest absolute energy reductions and, thus, had the shortest payback periods.

Chapter 3

Peel-and-Stick Electricity Meter for Panel Submetering

3.1 Introduction

In this chapter, the design and characterization of a Peel-and-Stick Electricity Meter (PASEM) sensor PCB built using Commercial Off-The-Shelf (COTS) components for metering individual circuit breakers is presented. A PASEM design based on commercially available components is practical for widespread adoption due to its standard PCB fabrication and assembly requirements. The sensor measures a circuit breaker's current *and* voltage with a 1 kHz analog front end bandwidth and 1920 Hz sampling rate. The system shows very good measurement performance and the PASEM can be built for a component cost below \$10 in moderate quantities. In the next section, an overview of each panel submetering hardware subsystem and the flow of sensor data will be discussed. A block diagram of the in-panel system can be seen in Figure 3.1, and a photo of a real installation in a lab with five metered breakers can be seen in Figure 3.2. The entire system is powered by one standard AC-DC converter plugged into a nearby power outlet.

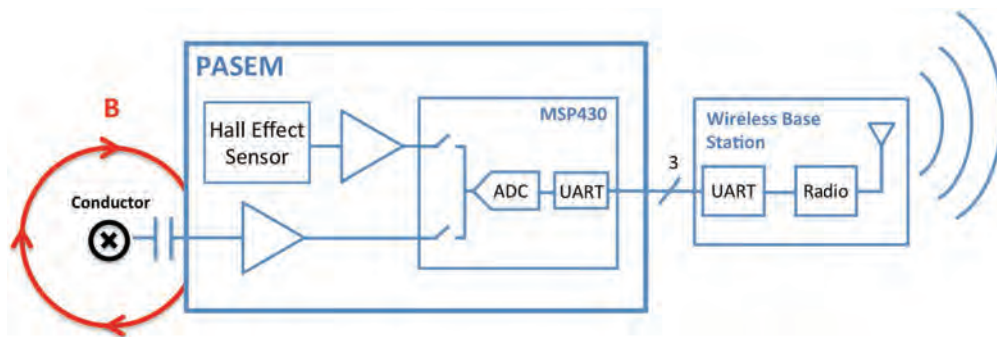


Figure 3.1: PASEM system block diagram showing sensing techniques, PASEM, and wireless base station.



Figure 3.2: PASEM system installation on circuit breaker panel. Five PASEM devices installed with wireless base station at bottom. Circuit breakers labeled for reference.

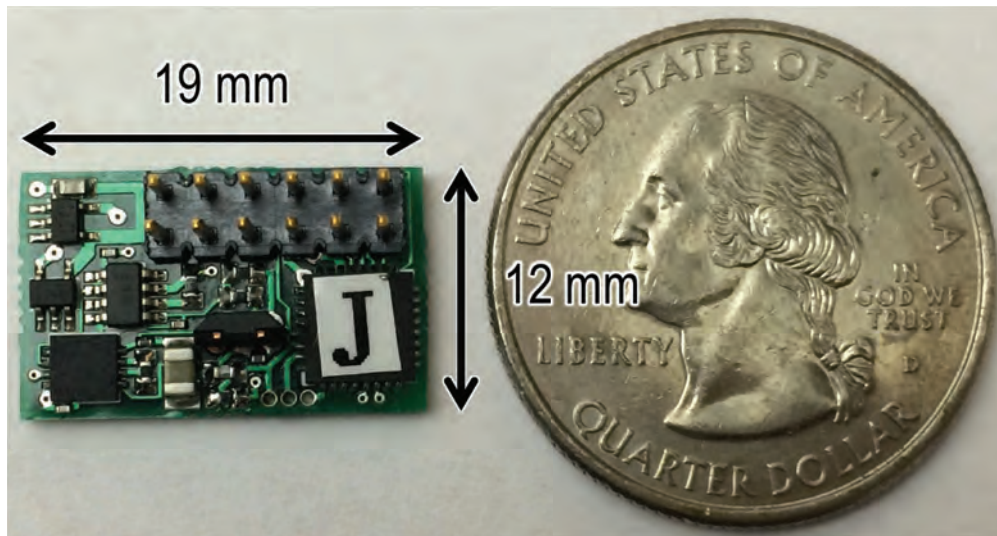


Figure 3.3: Assembled Peel-and-Stick Electricity Meter with US quarter dollar coin for size reference.

3.2 System Overview

PASEM Board

Each PASEM sensor board is equipped with an analog front end for current and voltage signal conditioning, as well as a Texas Instruments MSP430G2131 microcontroller. Details of the sensing and analog circuits will be discussed in Section 3.3. The entire PASEM board consumes around 16 mA average from a 5V supply. The current consumption is dominated by the Hall effect sensor, which consumes 10 mA. Potential future work to drastically reduce the power consumption is shown in Section 5.1. A close-up image of the 19 x 12 mm² assembled PASEM PCB board can be seen in Figure 3.3. The cost breakdown of the components on the PASEM PCB is shown in Table 3.1, quoted from large electronic component distributors for a quantity of 100 PASEM boards.

The PASEM's microcontroller is used for two purposes in the system: sampling the analog voltage and current sense signals, and transmitting samples to the wireless base station via a wired bus. To preserve information in the harmonics of the sensed current signals, a 1920 Hz sampling rate is used in the 10-bit microcontroller ADC. This sampling frequency was selected because it is a power-of-two multiple of the 60Hz fundamental line frequency, enabling straightforward computation of the fast Fourier transform (FFT) without aliasing. Thirty two samples (one 60 Hz cycle) of both the voltage and current sense signals are stored in the microcontroller's memory at all times. The sampled data from each PASEM sensor is sent over a UART serial link to the panel base station.

PASEM Component	Cost
Microcontroller	\$1.13
2x Amplifier ICs	\$3.21
2x Linear Voltage Regulator ICs	\$1.14
Hall Effect Sensor	\$1.04
Passives	\$1.83
2x6 Header Block	\$1.05
Total	\$9.40

Table 3.1: Simplified bill of materials for PASEM board.

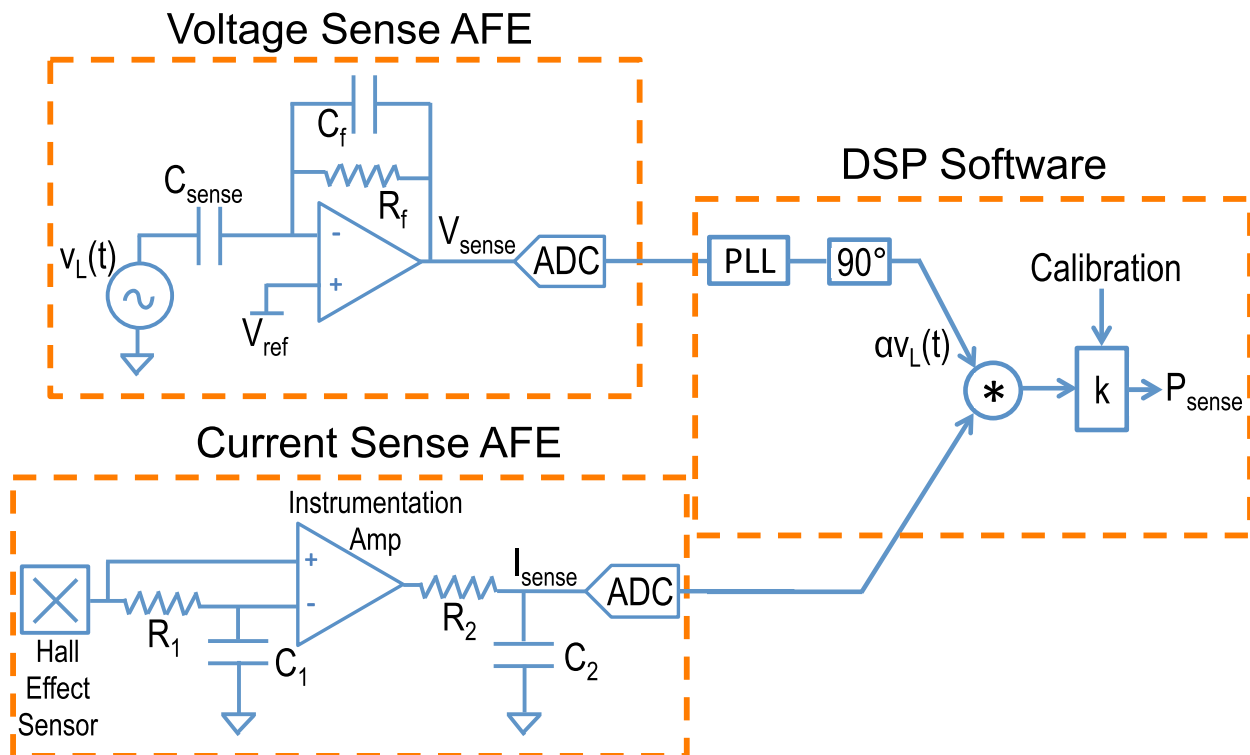


Figure 3.4: Signal processing block diagram showing current and voltage analog sensing circuits, and DSP real power calculation technique.

Wireless Base Station

In this system, a Raspberry Pi with custom adapter board functions as a base station for PASEM devices installed on the breaker panel. Python scripts run on the Raspberry Pi that manage the UART serial link. Voltage and current samples from the PASEMs are received by the wireless mote over the wired bus, and subsequently transmitted to a computer for further processing.

Laptop Computer

A laptop receives wireless data transmissions from the breaker panel wireless base station, and also performs subsequent DSP computations on the received samples. Python scripts are executed on the laptop that unpack the PASEM signals, calculate parameters of interest such as the metered breakers' line voltage signal and real power usage, and report the data to a cloud-based Simple Measurement and Actuation Profile (sMAP) server [30] for convenient viewing.

3.3 Sensing Implementation

Voltage Sensing

The analog circuits used in the capacitive voltage sensing scheme can be seen in Figure 3.4. The sense capacitance is essentially a parallel-plate capacitor formed between the bottom metal plane of the PASEM board and the conductor in the circuit breaker. For large capacitive coupling, careful PASEM board layout consideration was practiced to keep the bottom layer densely filled with metal. Assuming C_{sense} remains constant, the capacitor current can be monitored to obtain the time-derivative of the breaker's line voltage:

$$i_{sense} = C_{sense} \frac{dv_L(t)}{dt}$$

and if $\frac{1}{2\pi R_f C_f} \gg 60$ Hz:

$$V_{sense} \approx -R_f C_{sense} \frac{dv_L(t)}{dt}$$

Current Sensing

At the heart of the current sensing scheme is a Hall effect sensor that detects magnetic fields generated by currents flowing through a metered circuit breaker. The sensor used in this work is an SIP package A1301 Hall effect sensor by Allegro MicroSystems, with a 2.5 mV/Gauss sensitivity. A diagram of the current sensing analog circuitry is shown in Figure 3.4. Since the output of the hall effect sensor is single-ended, a reference needs to

be generated for the instrumentation amplifier’s inverting input. To create this reference, the output of the hall effect sensor is averaged by the $f_p \approx 0.3$ Hz R_1C_1 low-pass filter ($R_1 = 10k\Omega, C_1 = 47\mu F$). The amplified current sense signal is then passed through the $f_p \approx 1$ kHz R_2C_2 ($R_2 = 16\Omega, C_2 = 10\mu F$) anti-aliasing filter and is sampled at 1920 Hz by the microcontroller’s ADC.

Real Power Estimation

Figure 3.4 outlines the technique used to estimate real power once a circuit breaker’s I_{sense} and V_{sense} ($\frac{dv_L(t)}{dt}$) signals are obtained in the digital domain. To calculate real power, a signal representing the circuit’s line voltage, $v_L(t)$, must be determined. Assuming that $v_L(t)$ is sinusoidal, shifting the phase of the measured V_{sense} signal by 90° is analogous to integration. A software phase-locked loop was created in Python that tracks the phase of the V_{sense} signal, and synthesizes an ideal sinusoid with phase matched to $v_L(t)$, shown as $\alpha v_L(t)$ in Figure 3.4. Example measured I_{sense} , V_{sense} , and $\alpha v_L(t)$ signals can be seen in Figure 3.10a.

To calculate the instantaneous power waveform, $\alpha v_L(t)$ and I_{sense} are multiplied together. The mean of this instantaneous power signal provides an estimate of the real power dissipated in the circuit, in arbitrary units. A calibration constant must be found to map the power output of the system to real power in Watts. This calibration constant can be found by applying a known load to a submetered circuit while monitoring the software DSP real power estimator output. Assuming the PASEM boards’ analog circuits are well matched and the sensors can be placed in the same location on identical breakers, the calibration routine must only be performed once for every type of breaker to be metered. Once the calibration factors are determined, they are programmed into the laptop’s Python script for real-time data logging in units of Watts.

3.4 Experimental Results

In the characterization of the PASEM prototype, measurements were completed in a laboratory environment as well as in an actual residential installation. Figure 3.5a shows the internals of a common residential circuit breaker with a bimetallic strip trip mechanism. When the current through the breaker is large enough, the heat dissipated in the bimetallic strip causes a deflection that breaks the circuit. A second type of circuit breaker, which functions fundamentally differently, is shown in Figure 3.5b. The solenoid in this second type of circuit breaker concentrates the magnetic field in its surroundings, creating a magnetic force on nearby current-carrying conductors. As current increases past the breaker’s rated limit, the magnetic force becomes large enough to actuate the breaker. It is important to note that the breakers tested in this work are of the first type and do not contain solenoids, which would increase the magnetic field magnitude around the breaker by 10-20x. If solenoidal breakers were to be considered, the design of a high resolution current sensing system would be much

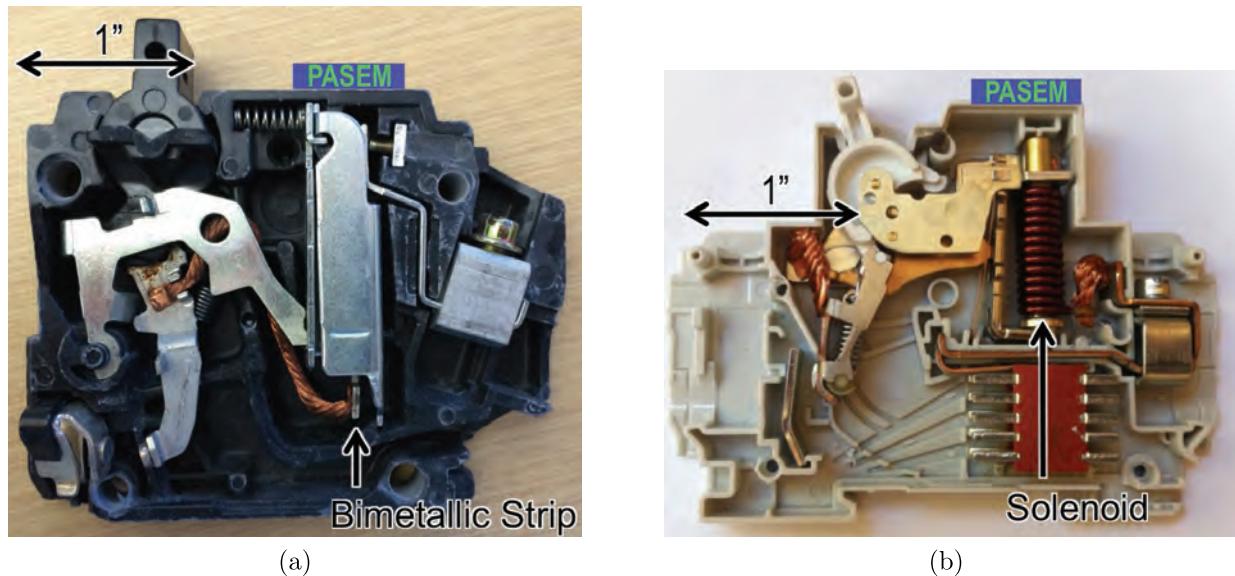


Figure 3.5: (a) Thermal-actuated circuit breaker innards with bimetallic strip and PASEM placement annotated. (b) Magnetic-actuated circuit breaker innards with solenoid and PASEM placement annotated.

easier due to the drastically increased signal-to-noise ratio (SNR). This work focused on the more challenging, but also more prevalent, thermally (thermal-magnetic) actuated circuit breakers. Investigations have shown that most thermal and thermal-magnetic breakers have internal geometries and current paths that are similar to Figure 3.5a.

Evaluation of Real Power Estimation Accuracy

To characterize the real power estimation performance of the PASEM sensor, its voltage and current sense outputs were monitored across a wide range of load currents. The test setup will now be described in detail. The PASEM device was powered by a 5V DC power supply and mounted onto the face of a circuit breaker in a bench top circuit breaker panel. The bench top panel is powered with a standard US power plug, which was plugged into the wall through a 20A power meter to provide reference power measurements. Incandescent lightbulb loads of various power ratings were switched on to load the breaker with different current magnitudes. The PASEM voltage and current sense signals were sampled with 16x averaging by an oscilloscope and subsequently processed in software to calculate real power. Figure 3.6 presents the results of this experiment, comparing the output of the PASEM sensor with the reference power meter. In this plot, the y-axis is a log scale, and measurement errors are less than 1% of full scale (1 kW) and typically less than 2% of measurement. From this plot, it is apparent that this sensing technique is effective, showing strong correlation with a reference meter down to load power levels below 10W.

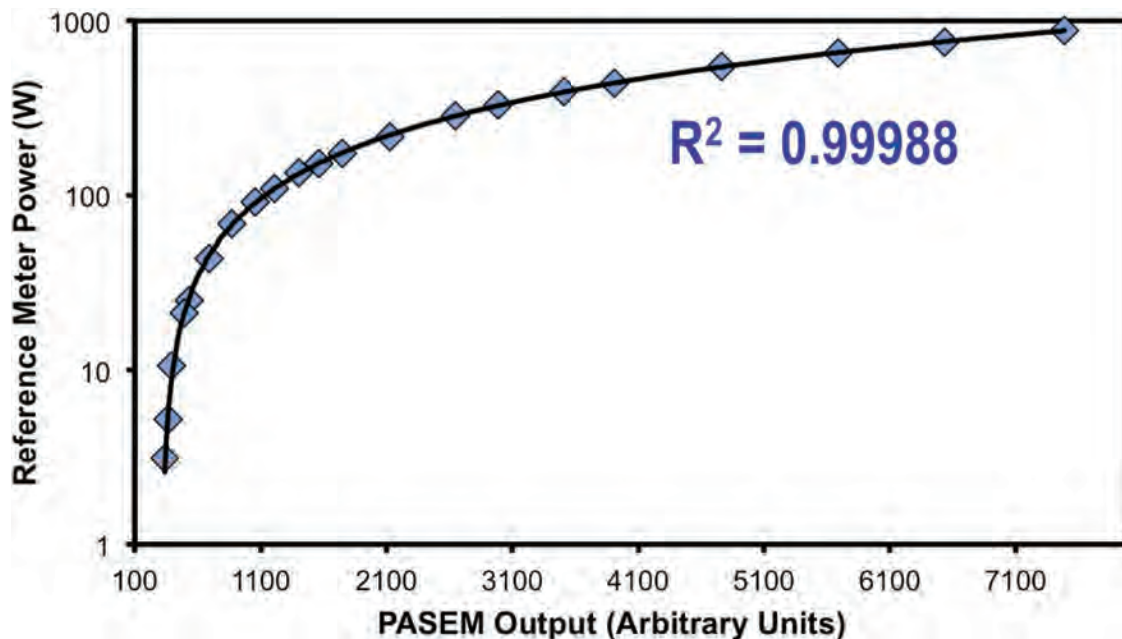


Figure 3.6: PASEM output vs. reference power meter, showing great correlation to sub-10W load powers.

Long-Term Capacitive Voltage Sensing Accuracy

Shown in Figure 3.7 is the line to neutral voltage vs. time in a 480V, 3-phase system, measured both with the PASEM V_{sense} circuit and a standard, contact-based reference voltage measurement. Considering this plot, it is apparent that the voltage in a building can change over time and it is important for the PASEM device to track this variation correctly. After a single point calibration of the PASEM’s V_{sense} to the contact-based measurement, the maximum error between the two measurements is always less than 1% of the reference reading. The PASEM system is able to track these changes in voltage, and the changes are automatically accounted for in the calculation of real power.

Current to Voltage Phase Error Characterization

Phase error between current and line voltage signals leads to error in the calculation of real power dissipation. Therefore, maintaining a small phase error between channels is critical in a power meter design. From AC power theory, the real power dissipated in a load is:

$$P_{real} = \frac{1}{T} \int_T v(t) i(t) dt = V_{RMS} I_{RMS} PF \quad (3.1)$$

PF is the power factor of the load, and for sinusoidal voltage and current waveforms:

$$PF = \cos(\theta_{load}) \quad (3.2)$$

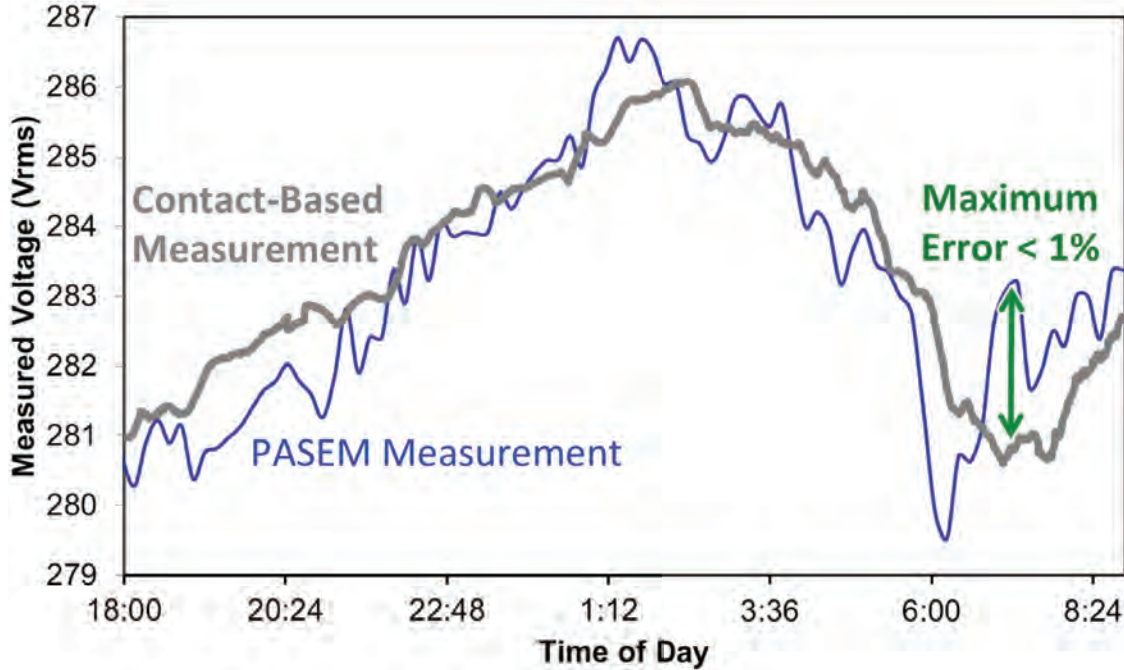


Figure 3.7: Long-term, 480V 3-phase line-neutral voltage measurement. PASEM analog V_{sense} output vs. contact-based measurement.

$$\Rightarrow \theta_{load} = \cos^{-1}(PF) \quad (3.3)$$

where θ_{load} is the load's current-voltage phase difference. The worst-case percent error in real power calculation due to an error in the current-voltage phase measurement is then:

$$\delta P_{real} = \delta PF = 1 - \frac{\cos(\theta_{load} + \theta_{error})}{\cos(\theta_{load})} \quad (3.4)$$

A plot of real power calculation error vs load power factor based on Equation 3.4 for various meter phase errors is shown in Figure 3.9. Real-world loads typically have power factors greater than 0.9 due to regulations and additional charges to customers with low power factor electricity draw.

To characterize the phase error of the PASEM meter, the following test was performed with the entire system installed in a full circuit breaker panel, as shown in Figure 3.2. With a resistive load applied to a metered breaker, the phases of the digitized I_{sense} and $\alpha v_L(t)$ signals were compared over many 60 Hz cycles. Raw data shows a systematic phase error of 1.6° , which was subtracted out as this can be accounted for in software when V_{sense} is shifted by (ideally) 90° to create $\alpha v_L(t)$. In Figure 3.8, a histogram of the phase difference between the PASEM's digital current and voltage signals is shown. The standard deviation of the phase error is 3.4° , and is likely due to amplitude noise on the V_{sense} and I_{sense} signals that leads to errors in phase estimation. As shown in Equation 3.4 and Figure 3.9, a 3.4° phase

error translates to 0.18% error in real power measurement for a resistive load (power factor = 1), and 3.05% error at power factor = 0.9. This is a promising result and is representative of the phase error introduced by all parts of the signal processing chain. The histogram appears to roughly follow a Gaussian shape. Thus, the effective phase error between current and voltage signals can be reduced by averaging over multiple cycles, which will subsequently minimize errors in real power estimation.

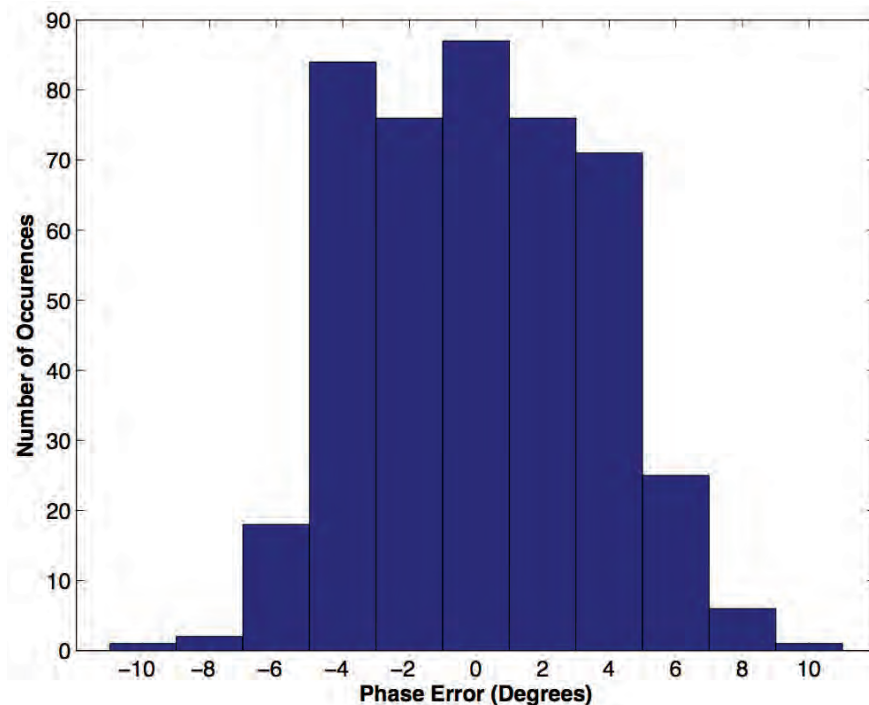


Figure 3.8: Measured current-voltage phase difference for a resistive load.

Performance with Non-Linear Loads

The outputs of the PASEM sensor with a resistive load connected through a TRIAC dimmer were examined to investigate how the sensor performs with a non-linear load. Figure 3.2 shows the test setup that was used for these measurements. The time domain waveforms measured during this test are shown in Figure 3.10a. These signals are shown with no averaging and were sampled at 1920 Hz using the PASEM's on-board microcontroller. It can be seen that abrupt changes in the circuit's current introduced by the TRIAC are tracked in the digitized I_{sense} signal. The frequency domain representation of the measured digital I_{sense} signal is also shown in Figure 3.10b. As expected, odd harmonics are prominent due to the TRIAC triggering events. This verifies the 960 Hz usable signal bandwidth resulting from the \approx DC to 1 kHz analog front end, and on-board PASEM ADC's 960 Hz Nyquist frequency.

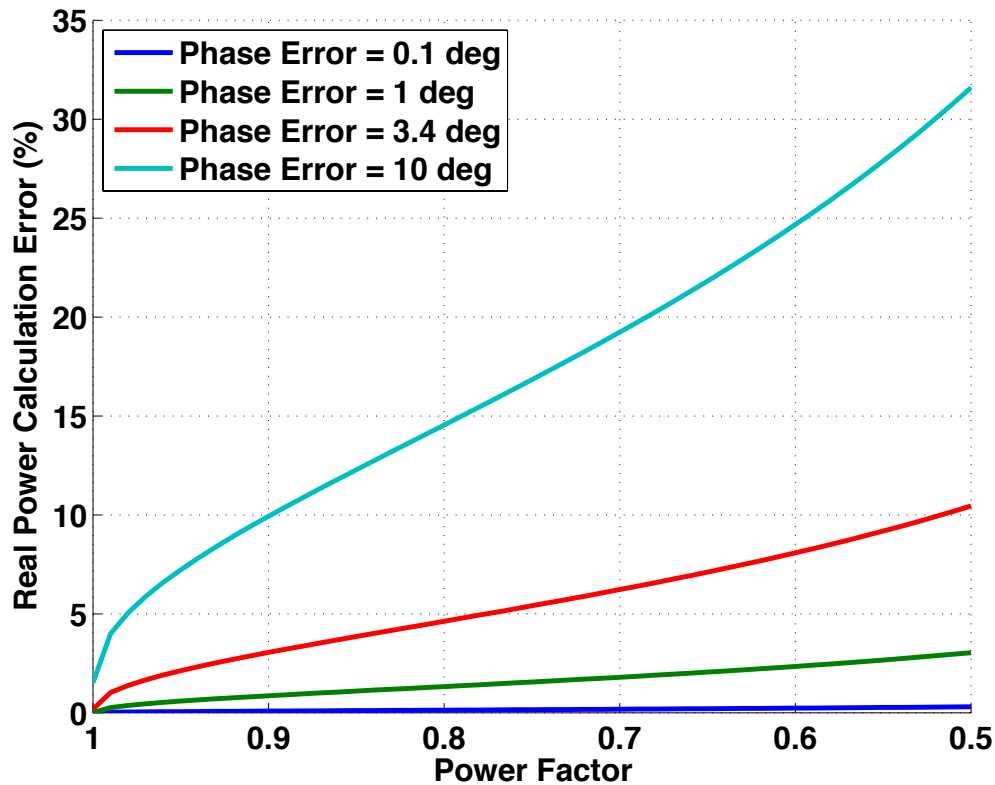
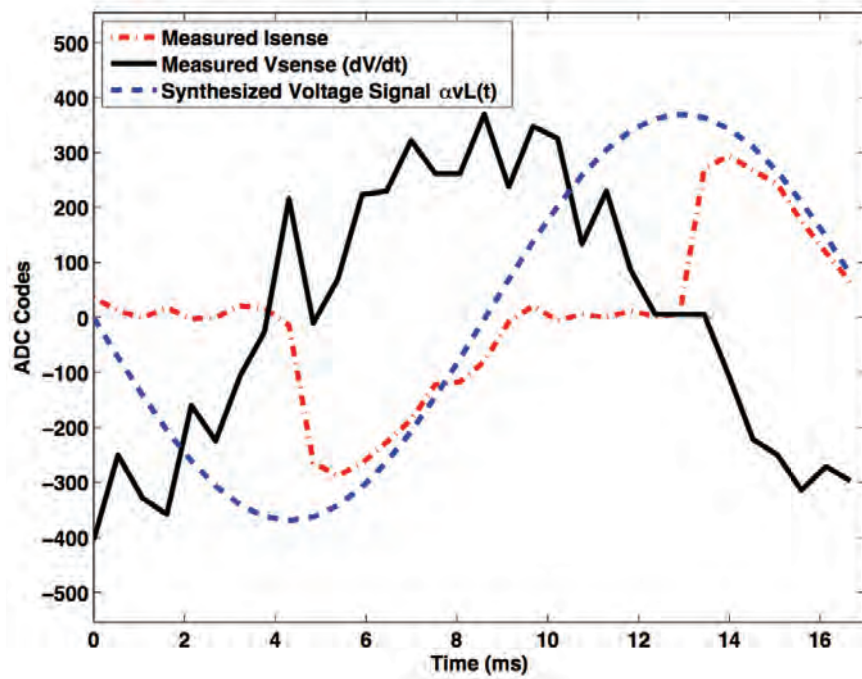


Figure 3.9: Real power calculation error vs. power factor for various phase errors. Real-world loads are typically designed to have $PF > 0.9$.

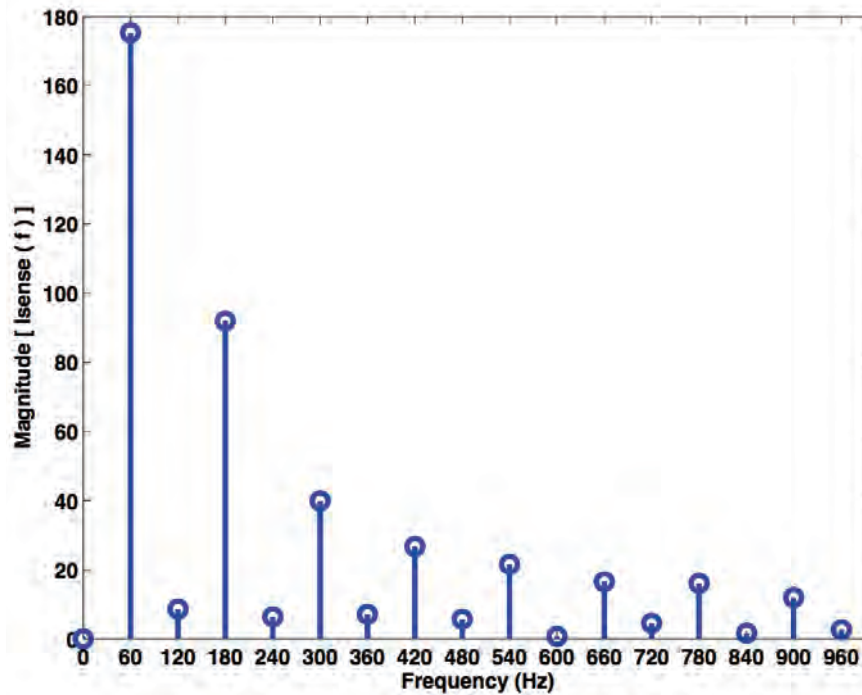
Residential Installation with Real Loads

The PASEM system was installed on a single breaker in a home to test the sensor in a real-world environment with various load types and transients. The breaker panel used for this test was also outfitted with a TED 5000 whole house meter to serve as a reference for calibration and measurement validation. During this experiment, the PASEM and base station were powered by a 5V DC power supply plugged into a wall outlet near the circuit breaker panel. A laptop receiving wireless PASEM sensor data, executing Python DSP software, and uploading data to an SMAP server was placed in a room adjacent to the breaker panel.

The PASEM was installed on the dwelling's kitchen circuit, which contains multiple appliances. Calibration of the sensor was completed by plugging different resistive loads into a kitchen wall outlet (with other loads static), and monitoring changes in the output of the PASEM and TED meter. A plot of the power data from both the PASEM-metered kitchen circuit and the reference TED meter over a period of 8 hours is shown in Figure 3.11. It can be seen that the PASEM sensor's measurement trends are consistent with the TED5000 meter when the various kitchen appliances are used. Differences in the trends of the two



(a)



(b)

Figure 3.10: (a) Sampled I_{sense} , V_{sense} , and phase-corrected line voltage signals for a TRIAC dimmer with resistive load. (b) FFT of sampled I_{sense} signal in (a).

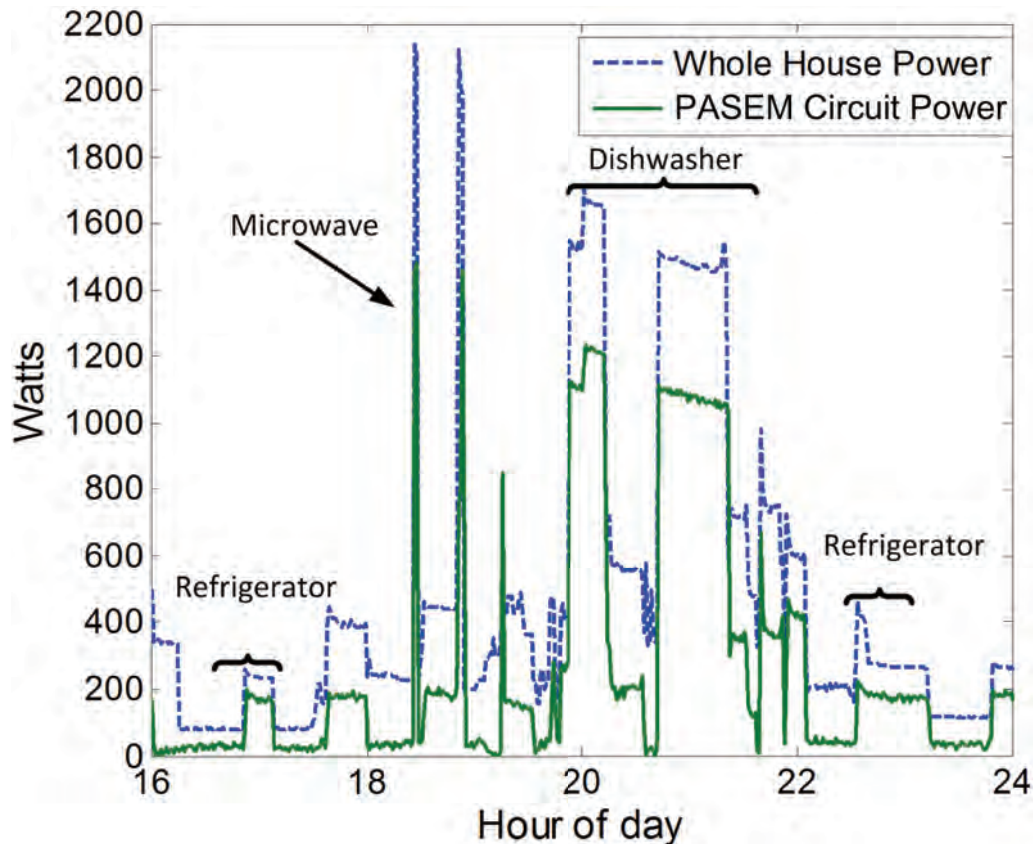


Figure 3.11: PASEM residential kitchen circuit vs. whole house meter data.

curves shown are due to load changes on other circuits in the residence. It is interesting to see that the kitchen circuit is often using over half of the total power dissipated in the duplex residence.

In-Panel Crosstalk Characterization and Correction

Shown in Figure 3.12 is an illustration that depicts how a PASEM's Hall effect sensor will detect magnetic fields from currents in adjacent circuit breakers, in addition to the breaker to which it is fastened. Hall effect sensors typically have one sensitive axis, and the output signal is proportional to the total resultant field from all sources in that direction. This results in erroneous estimates of the circuit breakers' currents. Figure 3.12 presents a simple case with current in three neighboring breakers, but this is only part of the picture. In a real installation, there may be tens of currents flowing nearby. The exact effects of this crosstalk are difficult to predict since the current path varies between breakers, which changes the shape of the magnetic vector field, and the geometry between circuit currents and PASEM sensors also changes from panel to panel. Therefore, accounting for the crosstalk is much more difficult than for the sensor system in Chapter 4.

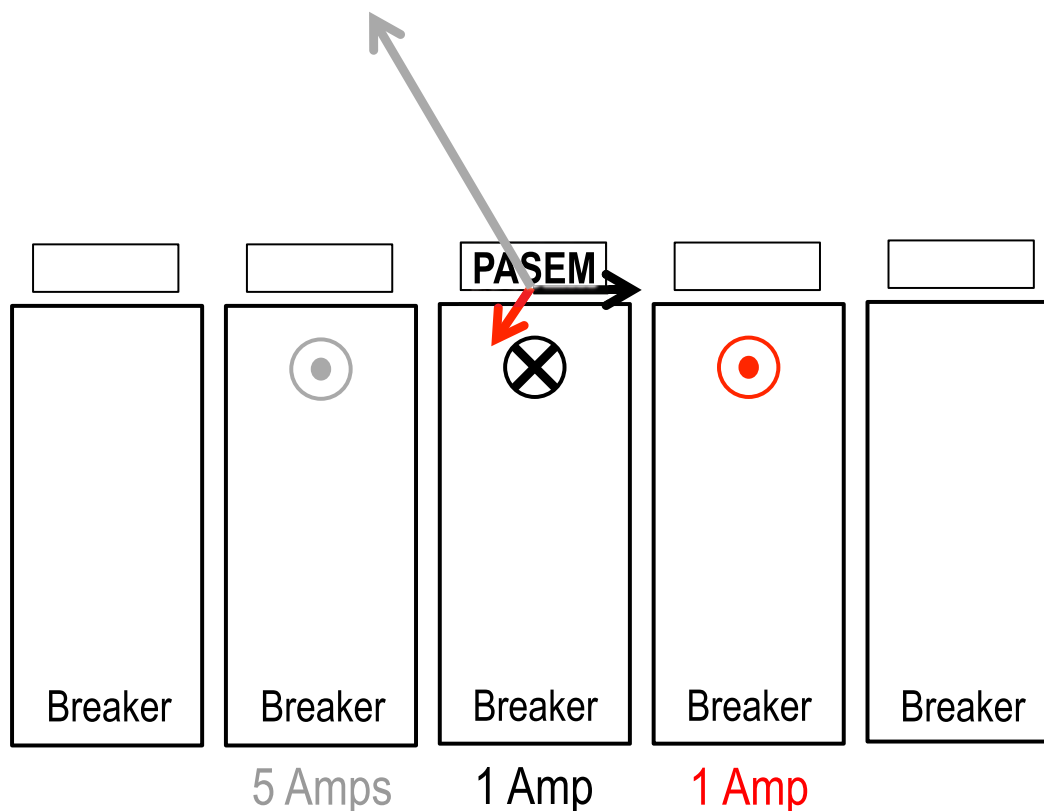


Figure 3.12: Circuit breaker panel crosstalk vector illustration.

Using the in-panel PASEM system installation shown in Figure 3.2, the signal crosstalk between neighboring circuits and sensors in the panel was characterized. With five sensors installed on consecutive breakers, the real power dissipation reported by all PASEMs was monitored with a resistive load applied to only the middle circuit. The results of this experiment can be seen in Figure 3.13. This circuit breaker panel is wired in a split-phase 120V/240V configuration resulting in a 180° phase difference between the line voltage of adjacent circuits. This causes the alternating positive/negative power measurements visible in Figure 3.13, however, the sign of the measured real power at sensor E is opposite what is expected. This is likely due to interference from other current-carrying conductors in the lower region of the breaker panel, highlighting a source of crosstalk besides the conductors inside the circuit breakers themselves. From this experiment, it is apparent that in-panel crosstalk from other conductors can lead to substantial errors in a circuit's real power estimation, and these effects must be accounted for to obtain valuable data in a real-world deployment.

Previous work in [17] showed that signals incident on the sensors from multiple conductors can be deconvolved to account for the current magnitude crosstalk between breakers. However, this technique requires applying a known load to every circuit in the panel to mea-

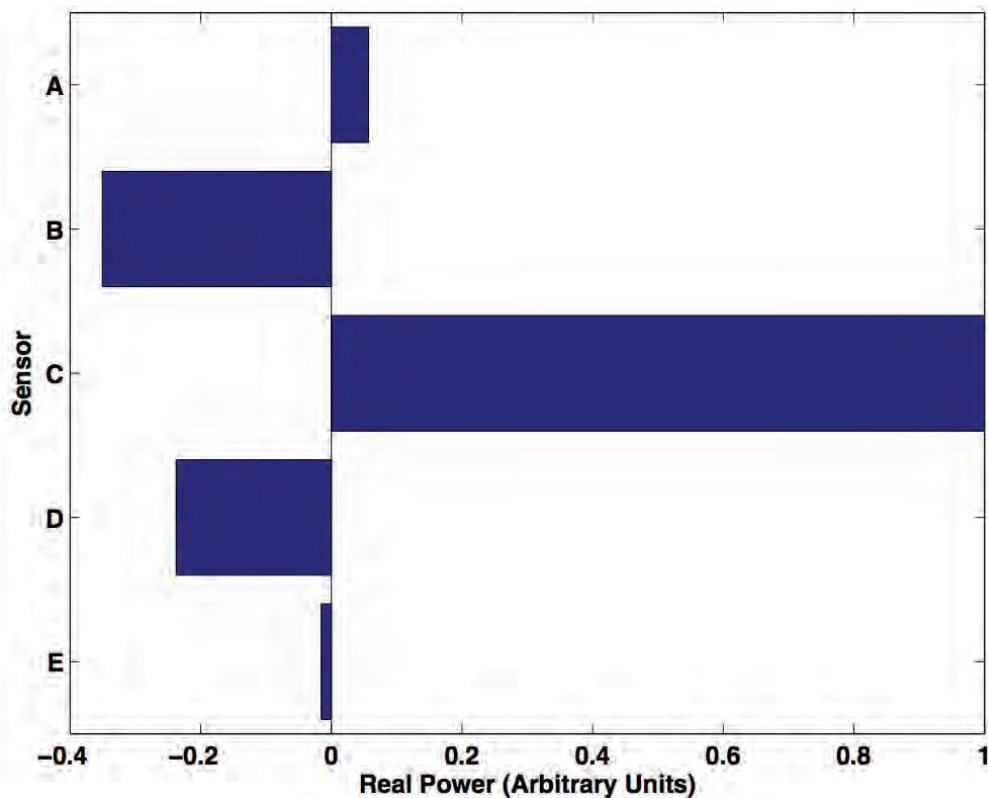


Figure 3.13: Real power measured by all five sensors due to a load on the center circuit.

sure the cross-sensitivity matrix, which can be a difficult and time-consuming task in a full installation. In [20], the authors built upon this technique and created a method to account for crosstalk that operates on the PASEM real power measurements and does not require manually measuring the cross-sensitivity matrix. This crosstalk cancellation method first uses the results from an electromagnetic simulation of a circuit breaker panel to estimate all breaker-to-sensor sensitivity parameters and provide initial crosstalk mitigation. If the types of circuit breakers in the panel are known ahead of time, this will lead to improved accuracy of the initial electromagnetic model. A statistical matching algorithm then monitors changes in multiple breaker signals simultaneously to improve the sensitivity matrix over time, further reducing errors due to the effects of nearby conductors on a circuit's power measurements. This technique was shown to be effective and resulted in average errors in real power measurement that were less than 5% after only a short learning period. The accuracy of the algorithm would increase as more data is examined over a long period of time. A hardware solution to improve the system's capability to account for these crosstalk effects is introduced in Section 5.2.

3.5 Comparison to State-of-the-Art

	This work [19], [20]	[15]	In-Panel Meters
Mfg Process	Standard PCB	Custom MEMS	PCB, ferromagnetics
Resolution	$\approx 80mA; 10W$	$\approx 100mA$	$< 1W$
Bandwidth	$f_{Nyquist} = 960$ Hz	RMS \rightarrow DC	
Outputs	I, V, Real Power	Current only	I, V, Real Power
Power	16 mA @ 5V	Zero	
Installed Cost	\approx \$10 per circuit	High	$>$ \$1000 per panel

Table 3.2: PASEM sensor comparison to state-of-the-art.

A table comparing the PASEM sensor system presented in this chapter to relevant work from academic literature and traditional in-panel circuit metering technology is shown in Table 3.2. Compared to the work in [15], the PASEM is able to measure line voltage, in addition to current, and calculate real power to provide more valuable AC power information. The PASEM system can be fabricated today for a low cost using commercially available components and PCB fabrication infrastructure, compared to the expensive custom MEMS process required by [15]. Traditional current transformer-based in-panel metering technologies are more accurate than the sensor presented in this work and also do not suffer from crosstalk issues. However, these in-panel systems have installation costs that are prohibitively high. With future algorithm and hardware development, the PASEM sensor system presented in this work could potentially match the accuracy of these traditional meters for a fraction of the required install cost and time.

Chapter 4

Plug-Through Energy Monitor for Wall Outlet Electrical Devices

4.1 Introduction

To help combat the fastest growing energy dissipator in buildings, a new type of sensor is needed that can ubiquitously meter plug loads and deliver continuous energy data that is disaggregated to end use. In the following sections, a plug-*through* energy monitor (PTEM) for plug load electrical devices is presented. This meter uses an inductive current sense coil printed directly into the PCB, resulting in a low-cost, low-power, wireless plug load meter that can be integrated into an outlet's faceplate for near-invisible metering hardware.

4.2 Inductive Current Sensing

To measure an electrical current, typically the circuit is broken, a series resistor is inserted in the loop, and the voltage across the resistor is monitored to measure the current according to Ohm's law. This technique is simple and effective, but has a number of drawbacks. Considering AC power meter applications, the sensor itself must be thicker than the blades of the plug (15.9 mm) in order to break the circuit and measure the current, leading to the clunky commercial meters available today. Power is also dissipated in the series current sense resistor, given by: $P = I_{load}^2 R_{sense}$. If $I_{load} = 10A$ and the sense resistor is $10\text{ m}\Omega$, the power dissipated in the resistor is $1W$; this is a substantial amount compared to the power required by the metering electronics.

In this work, inductive current sensing is used to measure the load current without breaking the load circuit loop. The physics governing this current sensing technique will now be discussed. When a current flows, it is accompanied by a rotational magnetic field as dictated by Ampere's Law:

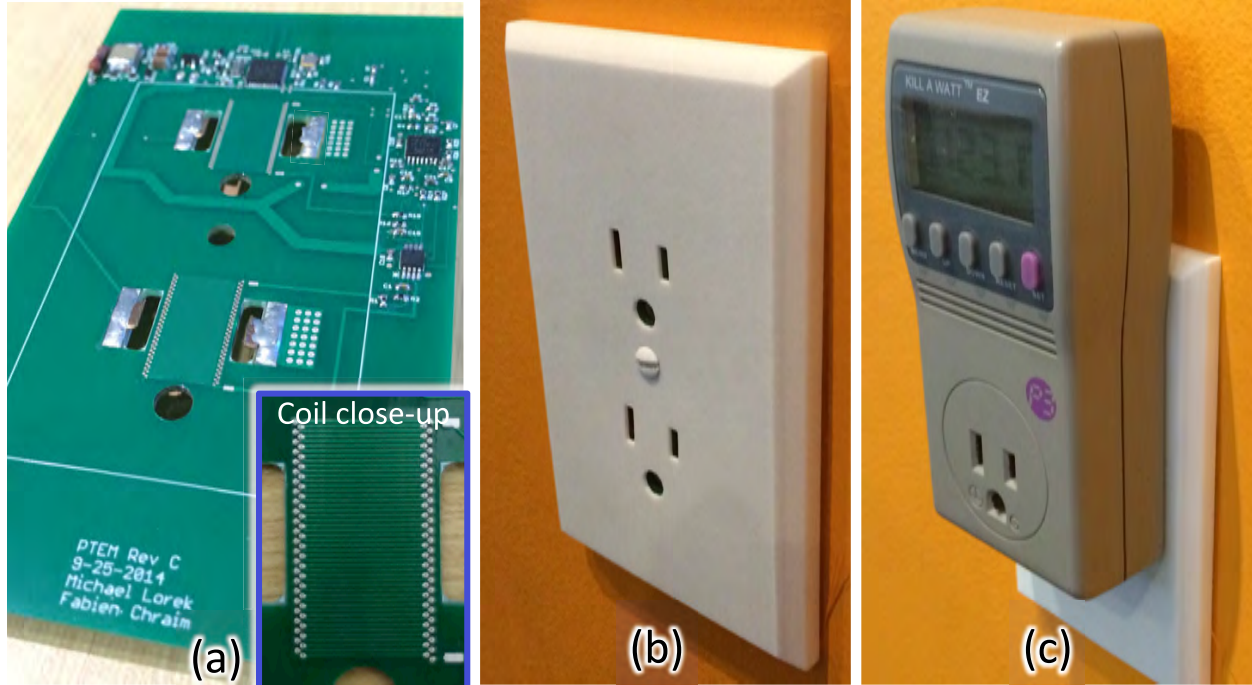


Figure 4.1: (a) PTEM sensor PCB. (b) PTEM installed on outlet with 3D-printed faceplate. (c) Kill A Watt EZ plugged into installed PTEM for size comparison.

$$\nabla \times \vec{H} = \vec{J} + \frac{\partial \vec{D}}{\partial t} \quad (4.1)$$

In addition, $\vec{B} = \mu \vec{H}$ is the magnetic flux density, and the magnetic flux through a surface S is given by:

$$\phi = \iint_S \vec{B} \cdot d\vec{s} \quad (4.2)$$

If the current is time-varying, the magnetic flux density, and, by extension, the magnetic flux, are also time-varying. As described by Faraday's Law and Lenz's law, a time-varying magnetic flux density is accompanied by a circulating electric field:

$$\nabla \times \vec{E} = -\frac{\partial \vec{B}}{\partial t} \quad (4.3)$$

Applying Stokes' theorem gives:

$$\oint \vec{E} \cdot d\vec{l} = -\frac{\partial \phi}{\partial t} = v_{emf} \quad (4.4)$$

Thus, if a loop of wire encircles a surface with a changing magnetic flux, the corresponding circulating electric field produces an electromotive force that is proportional to the time

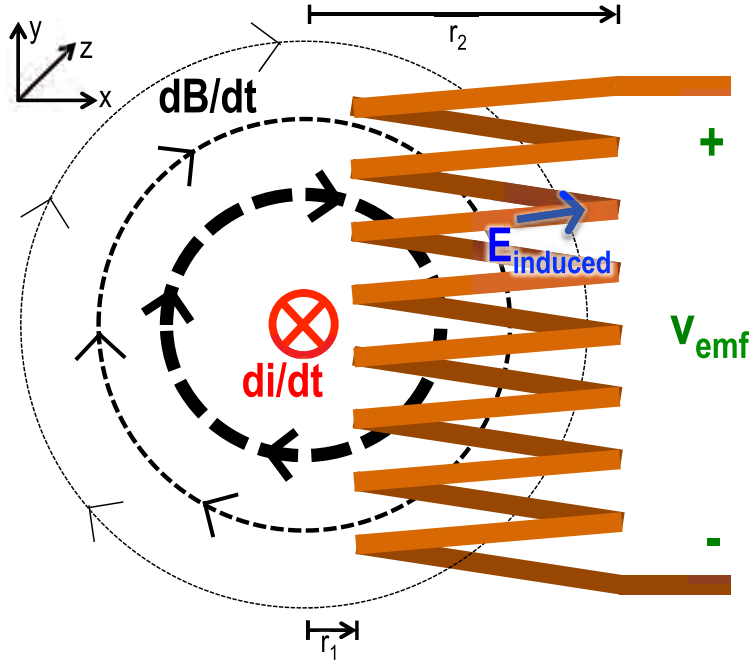


Figure 4.2: Inductive current sensing conceptual diagram.

derivative of the linked magnetic flux. Since the magnetic flux is linearly related to the flowing current, the voltage measured across the terminals of the wire loop is proportional to the time derivative of the current generating the magnetic field. This fundamentally creates a mutual inductance between the flowing current and the wire loop(s). In this power meter application, the mutual inductance between the load-current-carrying conductor and the sense coil on the PTEM sensor allows for the non-intrusive measurement of $\frac{di_{load}}{dt}$. For the ideal case of an infinite wire current:

$$v_{emf}(t) = -\frac{\partial \phi_{total}}{\partial t} = -\sum_{k=1}^N \left(\frac{\partial \phi}{\partial t} \right)_k = -2\frac{\mu \Delta_{z_{loop}}}{2\pi} \sum_{k=1}^N \left[\int_{r_1}^{r_2} \frac{x}{x^2 + y_k^2} dx \right] \frac{\partial i(t)}{\partial t} = M \frac{\partial i(t)}{\partial t} \quad (4.5)$$

where

$$M = \frac{\mu \Delta_{z_{loop}}}{\pi} \sum_{k=1}^N \left[\int_{r_1}^{r_2} \frac{x}{x^2 + y_k^2} dx \right] \quad (4.6)$$

with the load current infinite wire at (0,0,0) and the axes oriented as shown in Figure 4.2. Here N is the number of wire loops, $\Delta_{z_{loop}}$ is the depth of the wire loop in the z -direction, and y_k is the y -coordinate of the k^{th} wire loop.

4.3 Sensor System Design

Inductive current sensing offers two main benefits in the context of plug load meters. First, since the circuit does not need to be broken, the sensor itself can have a very slim profile, limited only by the thickness of the PCB and electronics. Also, the power dissipation of the sensor itself will be lower and independent of load current, since no voltage is dropped across a series sensing resistor. Figure 4.1 presents photos of the prototype PTEM sensor in comparison to the Kill A Watt EZ [21] meter that clearly show the improvement in form factor. The PCB was designed to meter both plugs in a common US duplex outlet so that some circuitry can be shared to reduce the cost per plug metered. This also allows the meter to integrate nicely with a plastic cover and act as a faceplate replacement. The system design details of the plug load meter will now be discussed.

The PTEM PCB is powered from the AC mains, and contacts the plug blades with sheet copper tabs soldered to the board. Due to the sensor's close proximity to a high voltage conductor, care must be taken to reduce capacitive coupling to the board by keeping impedances low. To reduce manufacturing costs, the PCB was designed with only two layers, and low cost components make the BOM around \$5 in large quantities. The RF performance of the sensor is very good - 802.15.4 packets are reliably received by a USB dongle at a range of ≈ 120 ft through multiple cubicles and walls. The power dissipation of the sensing and wireless communication electronics was measured to be 9.8 mA from a 3.6V supply when sending a 72-byte packet once per second. This is dominated by current draw associated with the microcontroller's oscillators and could be decreased by 10x with a board redesign.

PCB-Printed Inductive Sense Coil

With the current-carrying plug blades inserted through recesses in the PCB, the magnetic field lines form loops (infinite wire model) that are parallel to the plane of the board and governed by the right-hand rule. A vector field plot of the magnetic flux density in the region near the plug conductors and inductive sense coil is shown in Figure 4.3. This plot shows the resulting magnetic field due to both conductors when modeled as infinite wires and carrying the same current in opposite directions. Therefore, to sense this magnetic field using an inductive coil, the sensor coil must form loops with a surface normal vector that is parallel to the surface of the PCB. To create this helical structure, a series of traces and vias between the top and bottom metal layers was used. Compared to using a surface mount inductor for sensing, this approach allows the meter inline thickness to be only that of the PCB (vs. PCB + inductor¹). An 0402 inductor is ≈ 0.65 mm thick, or approximately 40% of the thickness of a standard PCB.

As evident in Figure 4.3, the magnetic field from the two current-carrying conductors add constructively in the region between the two plug blades. In order to obtain a stronger signal, and thus better signal-to-noise ratio, this is a natural place to place the inductive cur-

¹Assuming sense inductor placed as in [26]

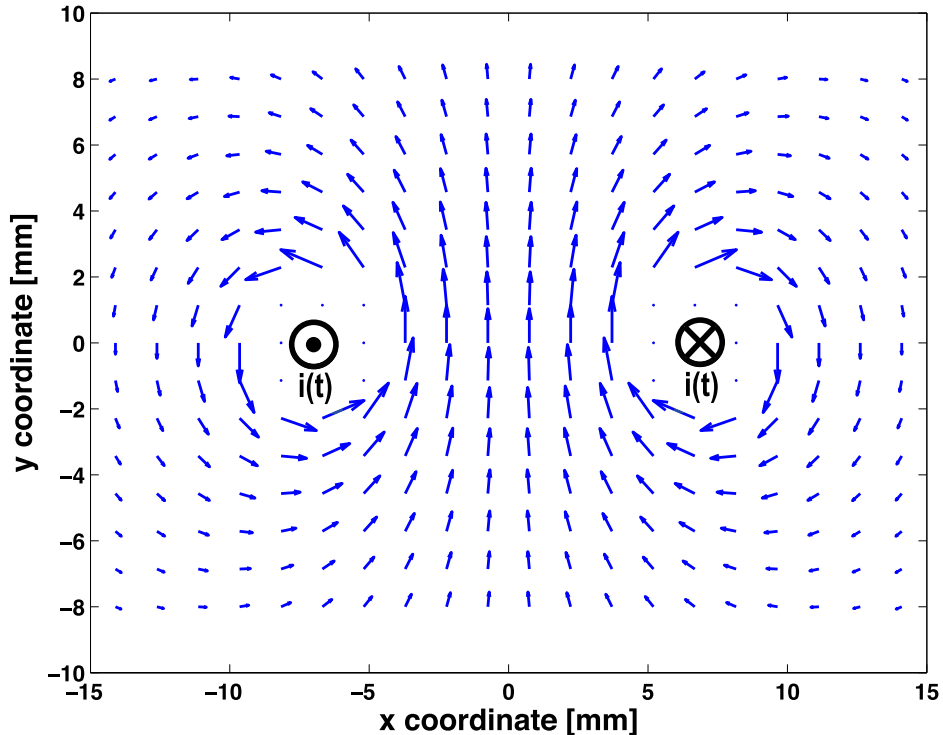


Figure 4.3: Magnetic flux density vector field plot around plug conductors and sense coil region. Model assumes infinite wire currents with locations annotated.

rent sensor coil. Figure 4.4 shows the total magnetic flux density y-component in the region between the plug blades, per Amp flowing through the load. The PCB-printed coil design used in this work can be seen in Figure 4.1(a). It has approximately 50 turns and measurements indicate that this design yields a mutual inductance of around 42 nH, compared to 31 nH as predicted by Equation 4.6.

Power Supply Circuits

The sensor PCB uses the circuit shown in Figure 4.5 to generate a stable DC voltage supply for the board’s electronics from the AC mains. When v_{Line} is decreasing, diode D1 connects node A to ground (neutral voltage), making $V_{C1} = -v_{Line,peak}$. During the other half cycle, diode D2 conducts and connects node A to node B. Assuming the Zener voltage is constant and the other diode voltage drops are negligible, the average current through D2 is:

$$i_{D2,avg} = C_1 (2v_{Line,peak} - V_{Zener}) f_{Line} \quad (4.7)$$

This current then splits between the LDO input and Zener diode, depending on the current draw of the electronics.

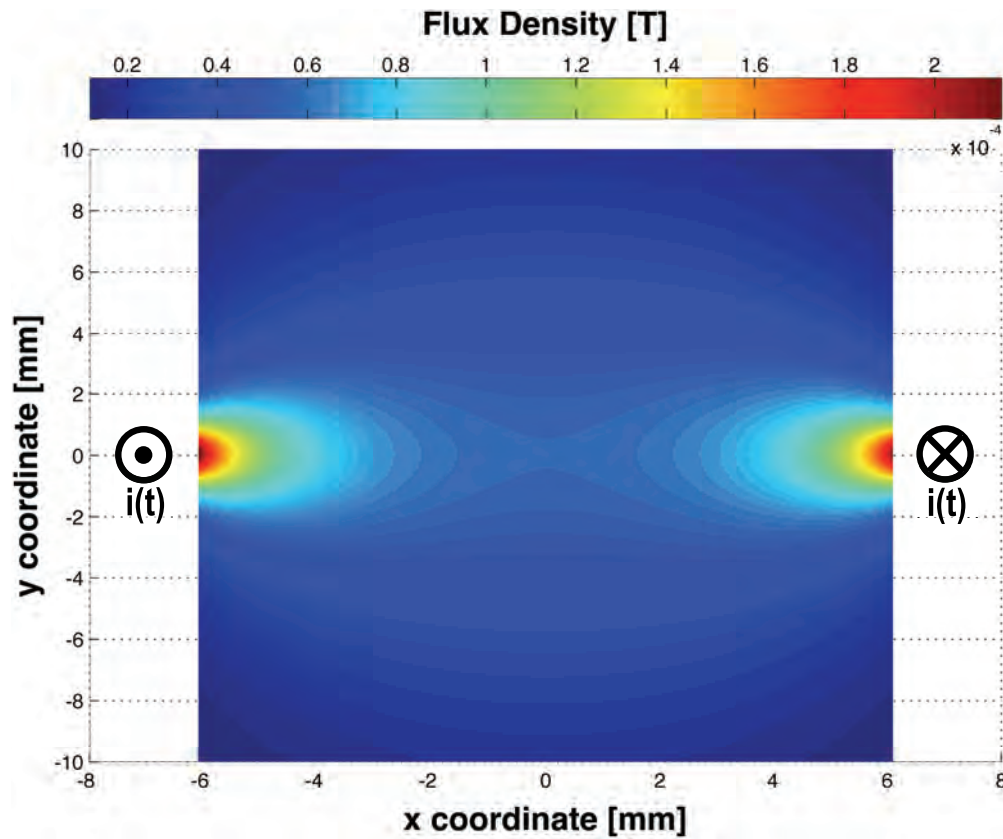


Figure 4.4: Spatial variation of B_y between plug conductors, per Amp through the load. Model assumes infinite wire currents with locations annotated.

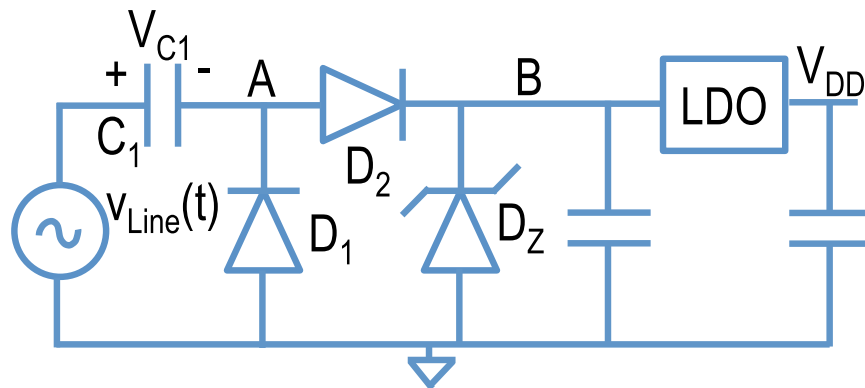


Figure 4.5: AC-DC converting power supply circuit.

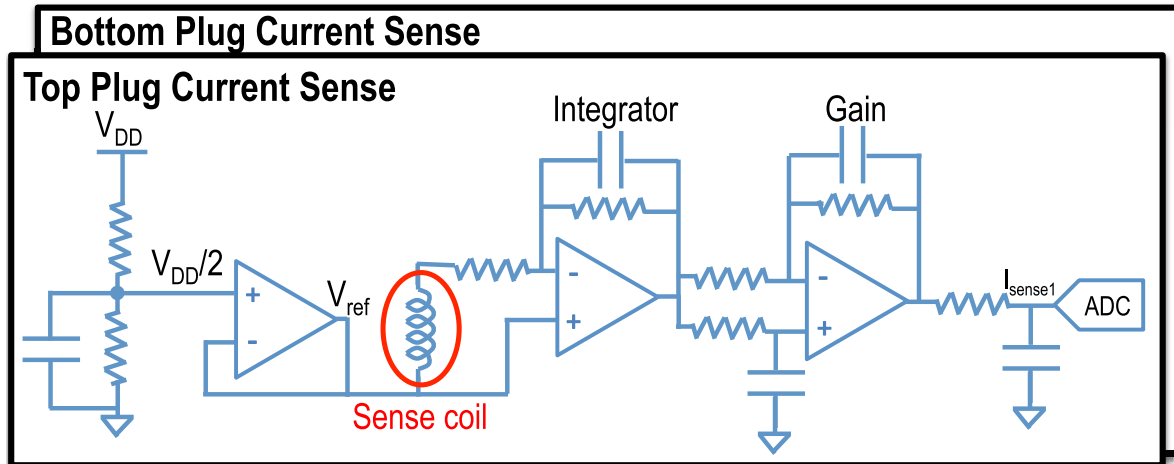


Figure 4.6: Inductive current sensing analog front end.

Microcontroller and RF

A CC2350 system-on-chip from Texas Instruments that includes an 8051 μ controller and 802.15.4 low-power radio is used in this sensor design. A folded dipole antenna is printed in the PCB, based on a reference design from TI. The onboard 14-bit sigma-delta ADC samples current and voltage measurement channels at 1920 Hz to keep harmonic content to 960 Hz. This gives the sensor the capability to measure non-linear loads accurately, and identify a load's harmonic content if desired. The embedded firmware is capable of performing averaging over multiple cycles to improve the signal-to-noise ratio of the measurement. To reduce power consumption, the microcontroller and radio go into a low-power mode, and wake up periodically to sample and transmit data. The signal averaging and sleep timers can be adjusted to change the transmitted sample rate.

Current and Voltage Sensing

The analog front end circuit used in the inductive current sensing scheme can be seen in Figure 4.6. The sense coil can be considered as a Thévenin equivalent source with $\approx 3\Omega$ resistance. At the frequencies of interest, the inductance of the sensor coil can be neglected. The first amplifier stage is a continuous time integrator, preceded by an inverting amplifier gain stage. An anti-aliasing filter precedes the ADC, with a cutoff frequency at approximately 1 kHz. There are two copies of this circuit on the board - one for each plug.

Since the sensor board contacts the line voltage directly, the load's voltage can be easily sensed with a resistive divider from the mains. The circuit used to sense the line voltage is shown in Figure 4.7. The bottom side of the resistor divider is biased by an opamp buffer at $\frac{V_{DD}}{2}$, which centers the divided line voltage waveform around the middle of the ADC range.

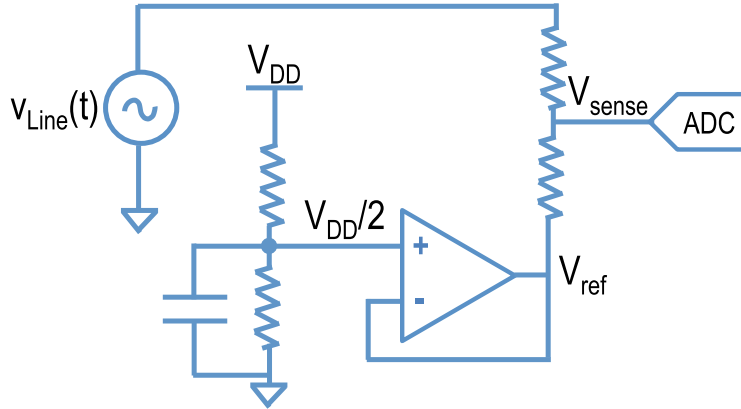


Figure 4.7: Line voltage sensing analog front end.

Laptop DSP Software

Sensor data is transmitted using the CC2530 radio to a laptop with an 802.15.4 USB receiver dongle. The time series data is received and processed in Python to calculate V_{RMS} , I_{RMS} , P_{real} , power factor and apparent power. For a large deployment, these metrics could be computed locally by the μ controller on each sensor node to reduce the load on the wireless network.

Crosstalk Cancellation

The total time-varying magnetic flux, $\frac{\partial \phi}{\partial t}$, linking each inductive sense coil is due to a vector summation from all sources of time-varying magnetic fields. In this case, the two main sources are the AC currents flowing through each plug in the duplex outlet. Ignoring other sources of magnetic field, this can be represented by the following inductance matrix:

$$\begin{bmatrix} v_{coil_1} \\ v_{coil_2} \end{bmatrix} = \begin{bmatrix} M_{1,1} & M_{1,2} \\ M_{2,1} & M_{2,2} \end{bmatrix} \begin{bmatrix} \frac{\partial i_{load_1}}{\partial t} \\ \frac{\partial i_{load_2}}{\partial t} \end{bmatrix} \quad (4.8)$$

where v_{coil_1} and v_{coil_2} are the top and bottom coil voltages, i_{load_1} and i_{load_2} are the top and bottom plug currents, and the M terms are material and geometry dependent parameters. After integration in analog hardware, the sampled signals available to the onboard microcontroller are:

$$i_{sense_1} = \int \left(M_{1,1} * \frac{\partial i_{load_1}}{\partial t} + M_{1,2} * \frac{\partial i_{load_2}}{\partial t} \right) dt = a * i_{load_1} + b * i_{load_2} \quad (4.9)$$

$$i_{sense_2} = \int \left(M_{2,1} * \frac{\partial i_{load_1}}{\partial t} + M_{2,2} * \frac{\partial i_{load_2}}{\partial t} \right) dt = c * i_{load_1} + d * i_{load_2} \quad (4.10)$$

The constants of integration can be ignored here, as the electronics keep the analog signals centered around $\frac{V_{DD}}{2}$. Equations 4.9, 4.10 can then be put in the following matrix form:

$$\Rightarrow \begin{bmatrix} i_{sense_1} \\ i_{sense_2} \end{bmatrix} = \begin{bmatrix} a & b \\ c & d \end{bmatrix} \begin{bmatrix} i_{load_1} \\ i_{load_2} \end{bmatrix} \quad (4.11)$$

Once the a, b, c, d parameters are known, this matrix relationship can be inverted to deconvolve the two load currents from the signals measured at both sensor coils:

$$\Rightarrow \begin{bmatrix} i_{load_1} \\ i_{load_2} \end{bmatrix} = \begin{bmatrix} a & b \\ c & d \end{bmatrix}^{-1} \begin{bmatrix} i_{sense_1} \\ i_{sense_2} \end{bmatrix} = \begin{bmatrix} \alpha & \beta \\ \gamma & \delta \end{bmatrix} \begin{bmatrix} i_{sense_1} \\ i_{sense_2} \end{bmatrix} \quad (4.12)$$

$$\Rightarrow \begin{aligned} i_{load_1} &= \alpha i_{sense_1} + \beta i_{sense_2} \\ i_{load_2} &= \gamma i_{sense_1} + \delta i_{sense_2} \end{aligned} \quad (4.13)$$

The geometry between the sensors and conductors remains fixed, thus, the $\alpha, \beta, \gamma, \delta$ parameters can be calculated by matrix inversion offline only once (based on measurement of a, b, c, d), and then programmed into firmware/software. The sensor system can then compute these simple arithmetic operations in real-time to perform crosstalk cancellation during data acquisition. This is similar to the idea presented in [17] and Section 3.4, except the technique is more easily and effectively implemented since the geometry between conductors and sensors is the same in all installations in this case.

4.4 Experimental Results

Laboratory Characterization

Calibration and Accuracy

In order to measure the a, b, c, d calibration coefficients in Equation 4.11, the following procedure was performed. A current transformer connected to an oscilloscope served as a reference current measurement. For each test case, the current transformer output and PTEM's i_{sense_1} and i_{sense_2} signals were logged simultaneously over a ten minute period. To determine the coefficients, a best fit line was plotted between the two variables. The slope provides the calibration factor used to convert the current measurement channel's ADC output from units of ADC codes to units of Amps. While sweeping i_{load_1} with $i_{load_2} = 0$, coefficients a and c can be determined:

$$a = \left. \frac{i_{sense_1}}{i_{load_1}} \right|_{i_{load_2}=0} \quad (4.14)$$

$$c = \left. \frac{i_{sense_2}}{i_{load_1}} \right|_{i_{load_2}=0} \quad (4.15)$$

Next, by sweeping i_{load_2} with $i_{load_1} = 0$, coefficients b and d are found:

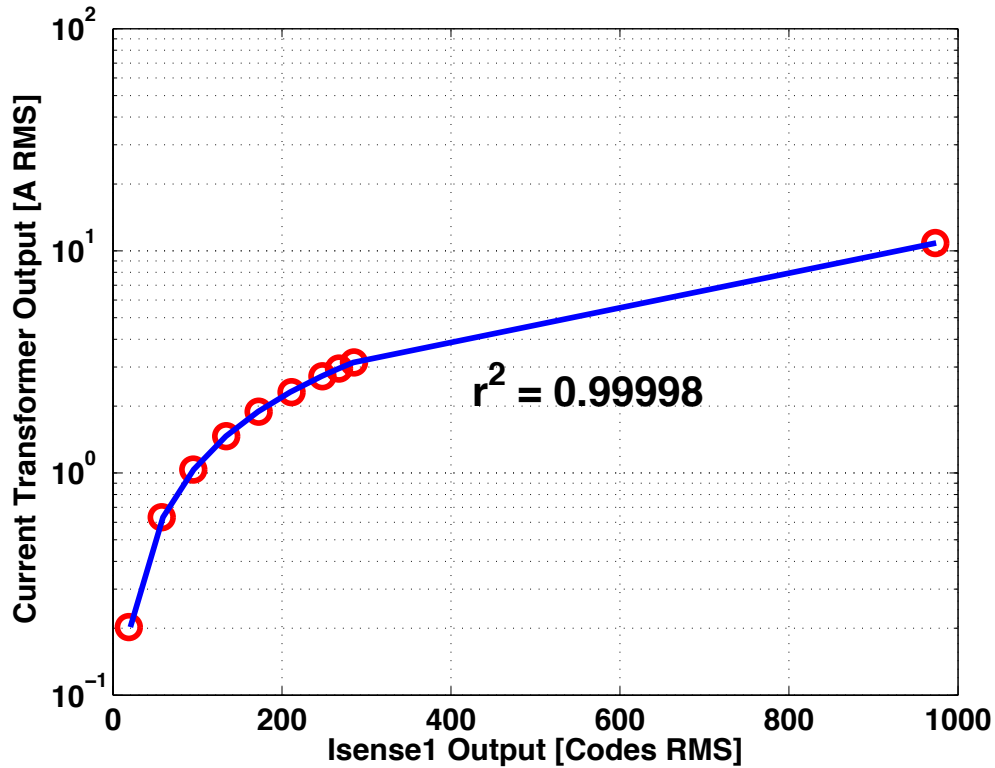


Figure 4.8: PTEM i_{sense_1} vs. current transformer for various i_{load_1} , with $i_{load_2} = 0$.

$$b = \frac{i_{sense_1}}{i_{load_2}} \Big|_{i_{load_1}=0} \quad (4.16)$$

$$d = \frac{i_{sense_2}}{i_{load_2}} \Big|_{i_{load_1}=0} \quad (4.17)$$

A plot of the measured data and best-fit line for the self-sensitivity of i_{load_1} to i_{sense_1} (coefficient a) is shown in Figure 4.8. The correlation of determination for the data was computed, and the r^2 value is very close to 1, verifying that the sensor output matches the current transformer very well across a range of currents. The standard deviation of the PTEM's current measurement is typically a factor of 100-1000 smaller than the mean. Measuring the noise of the system with no load current, the $\mu + 3\sigma$ noise is ≈ 20 mA RMS, corresponding to 2.4W with 120 V RMS mains and unity power factor.

To calibrate the PTEM voltage measurement channel, a Watts Up Pro [31] meter was used as a reference voltage meter. The voltage data from the Watts UP Pro and PTEM's v_{sense} signal were logged simultaneously over a period of 10 minutes, and the ratio of the mean values was used to find the voltage channel calibration coefficient. This coefficient only needs to be measured once, and then programmed into software or firmware.

Inductive Current Sensor Analog Front End Bandwidth

Shown in Figure 4.9 are sampled waveforms from the output of the PTEM sensor with a resistive load connected through a TRIAC dimmer. The TRIAC dimmer creates sharp transitions in the current waveform when it switches, introducing significant harmonic content into the current waveform. In the middle plot, it is visible that the PTEM is able to track the changes quickly when the TRIAC switches. The bottom plot shows the FFT of the current waveform, with signal content up to the 960 Hz Nyquist frequency.

Entertainment Center Metering

In order to test the prototype sensor with real world loads, the PTEM was installed on an outlet with six electronic devices connected via a power strip. The connected loads were: a cable modem, wireless router, digital cable box, 40" LCD TV, AV receiver, and Xbox One. The Watts Up Pro meter was also configured to measure and log the AC power parameters of this outlet for comparison. The power time series data from this test is shown in Figure 4.10. The traces are shown with smoothing over ≈ 30 seconds to reduce high-frequency fluctuations and highlight longer-term trends in the power data.

While the traces from the PTEM and Watts Up Pro both have the same shape, the Watts Up Pro meter is consistently reporting a higher value. Examining the voltage, current, and power factor datasets from both meters, it is clear that this disparity is due to a difference in the meters' current measurements. Applying a scaling factor of 1.16 to the PTEM current reading makes the two power time series match almost perfectly. It is unclear whether the erroneous current measurement is from the Watts Up Pro or the current transformer that was used as the PTEM's current calibration reference.

Crosstalk Cancellation

The effectiveness of the crosstalk cancellation algorithm was tested by applying a sequence of loads to both the top and bottom plugs and monitoring the estimates of i_{load_1} and i_{load_2} , with and without the algorithm presented in Equations 4.12 and 4.13 activated. Figure 4.11 shows the measured i_{load} signals compared to the actual load currents without the deconvolution algorithm enabled. From these plots, it is apparent that the error due to crosstalk is substantial - an error of approximately 0.5 A is introduced on i_{load_1} when there is an 11 A load applied to i_{load_2} slightly before the 4 minute mark. This error remains when $i_{load_1} \rightarrow 0$ around $t = 5.8$ minutes. Crosstalk in the opposite direction is also visible when i_{load_1} changes, although the effect is less noticeable on i_{load_2} due to the disparity in currents.

Figure 4.12 presents the same time series of data with the crosstalk cancellation algorithms enabled. It is clear that the technique is effective; the large errors on i_{load_1} are now much reduced. While the measured traces in Figure 4.12 do not match the ideal load currents exactly, the accuracy can likely be improved by better measurement of the a, b, c, d parameters in Equation 4.11 with a more repeatable test setup.

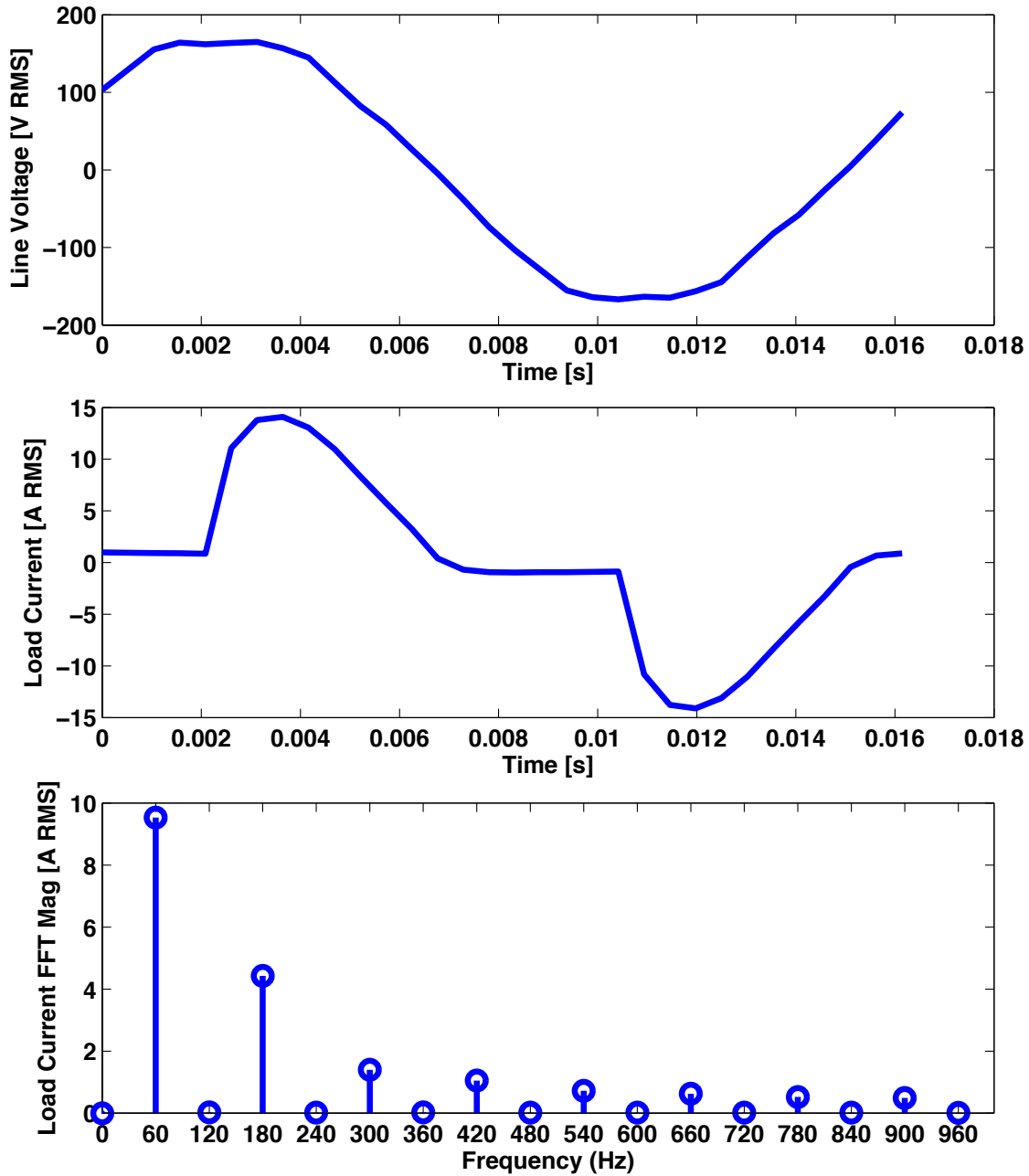


Figure 4.9: TRIAC dimmer with resistive load; top: $v_{sense}(t)$, middle: $i_{load_1}(t)$, bottom: $\text{FFT}[i_{load_1}(t)]$.

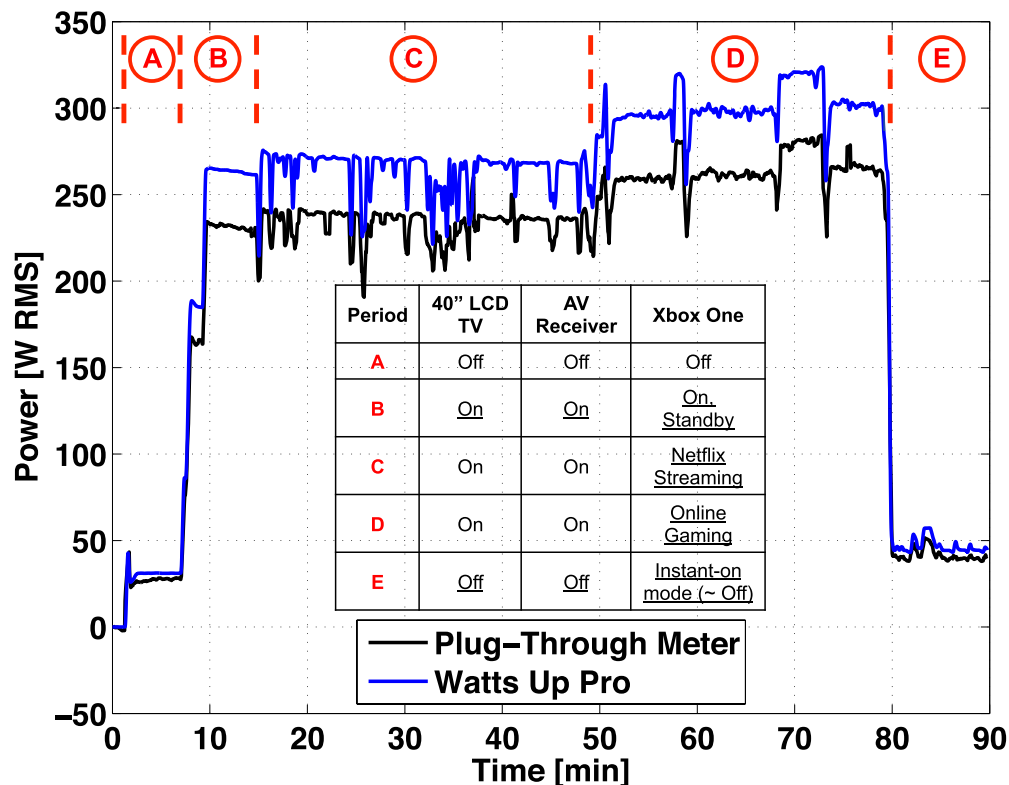


Figure 4.10: Entertainment center power timeseries with ≈ 30 second smoothing. Digital cable box, cable modem, and wireless router always on.

4.5 Comparison to State-of-the-Art

Although their PowerBlade sensor is also based on non-intrusive current measurement, the authors in [26] took different approaches to multiple aspects of their plug load power meter design. First, considering the form factor, they designed a sensor that is arranged in a plug-through manner between a plug and wall outlet, but it is meant to be associated with the load itself and to be moved from outlet to outlet. While this makes it easier to associate a stream of sensor data with a specific plug load, it could also be troublesome. First of all, the sensors need to be moved around and kept track of, compared to the PTEM which is “out of sight, out of mind” at all times after a simple, quick installation. In a commercial environment, different people are coming and going all the time, often bringing various plug loads to and from home, and it would be difficult to meter all of these loads using the PowerBlade.

Compared to the 802.15.4 wireless communication protocol used in the PTEM design, the PowerBlade’s use of Bluetooth Low Energy (BLE) is less amenable to large-scale deployments that aim to meter all outlets in a building. The 802.15.4 protocol, network stack, and accompanying hardware have been in development for many years to optimize wireless mesh

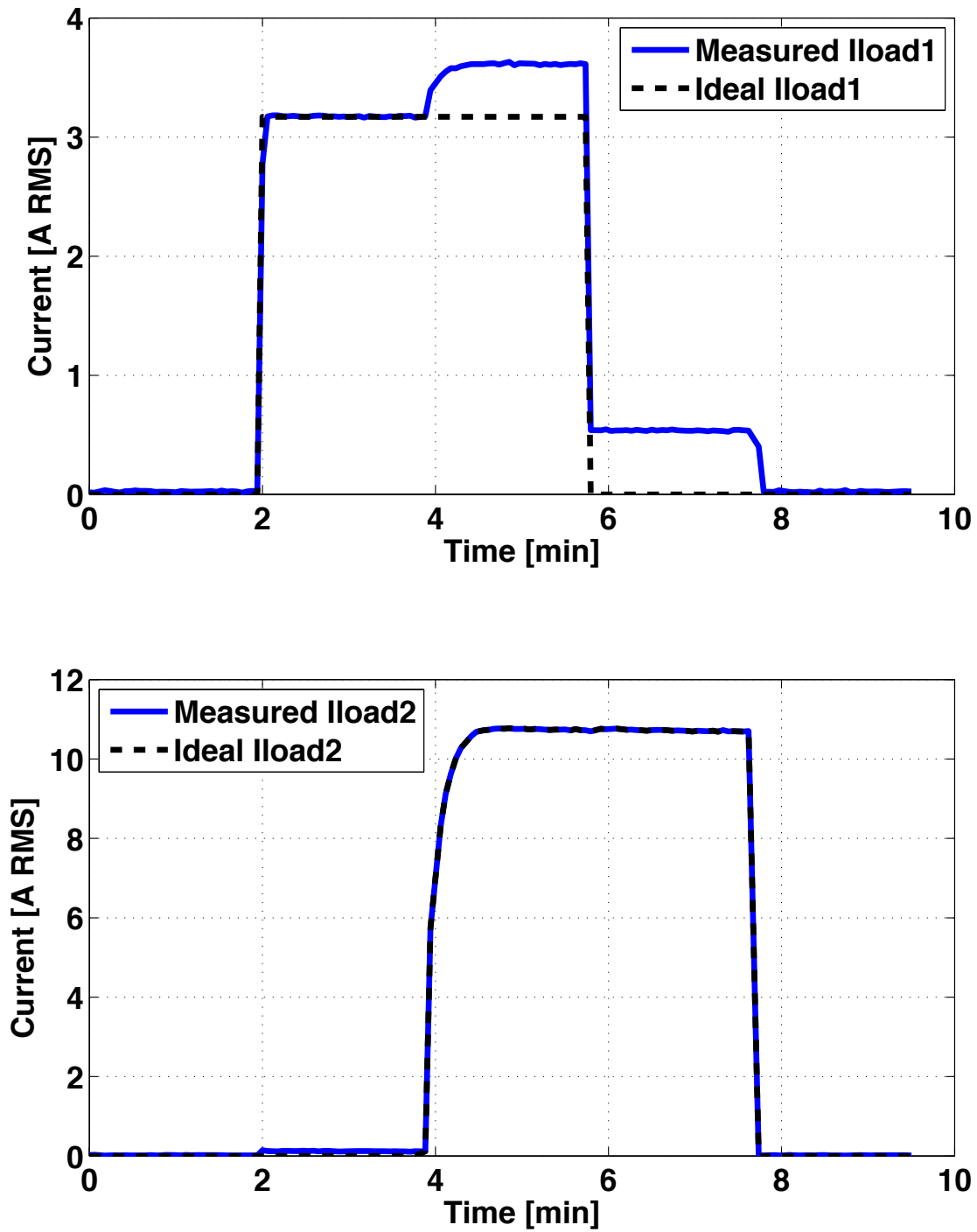


Figure 4.11: i_{load_1} and i_{load_2} signals. No crosstalk cancellation algorithm.

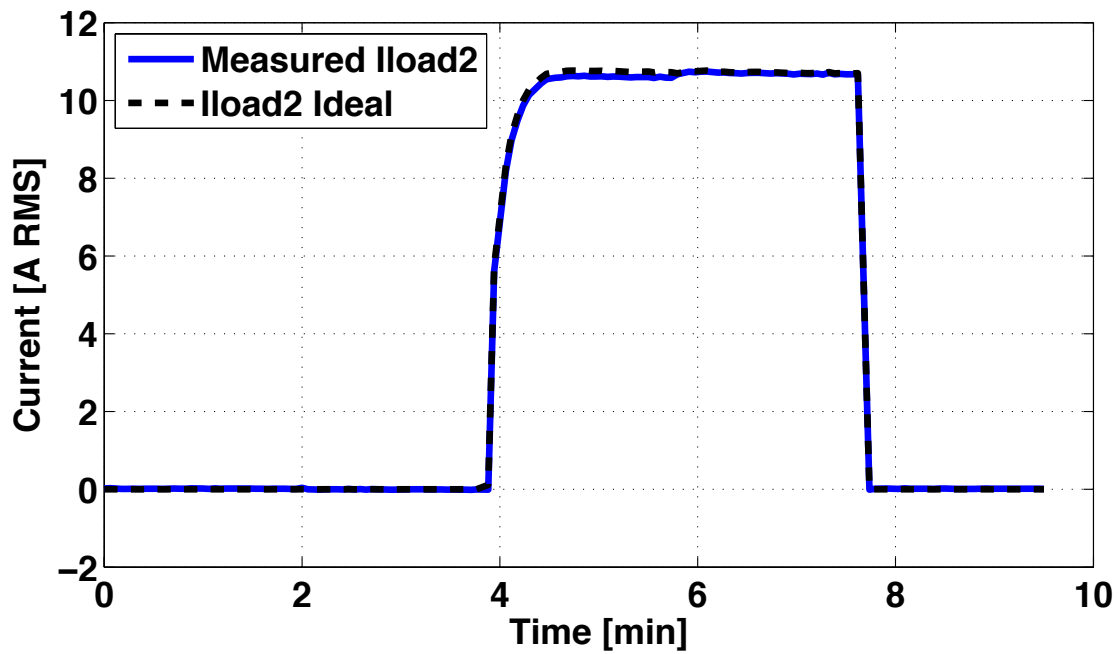
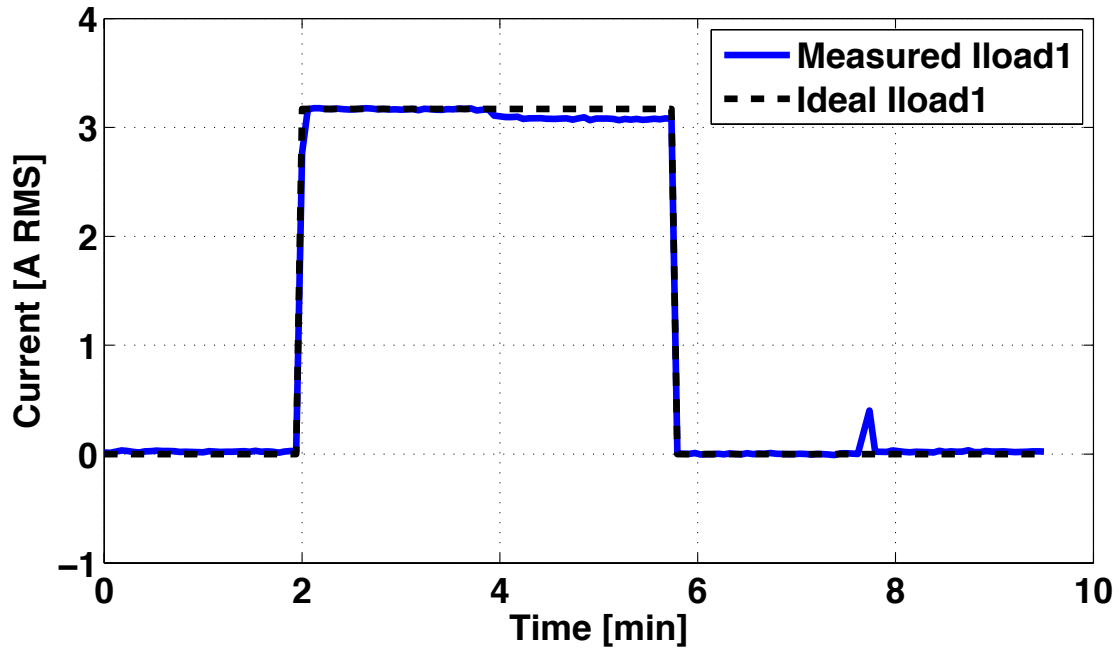


Figure 4.12: Deconvolved i_{load_1} and i_{load_2} signals. Crosstalk cancellation algorithm active.

networking in applications just like this. The technology enables these networks to support thousands of devices and send packets with $\approx 99.999\%$ delivery rates. The sensor nodes can also operate with very low radio energy budgets due to radio duty cycling enabled by time synchronized channel hopping [32]. The BLE wireless communication employed in PowerBlade is more suitable for smaller numbers of nodes and point-point communication.

Overall, the PowerBlade sensor is appropriate for applications similar to today’s commercial meters, instead of what is targeted in this work: ubiquitous monitoring of all plug loads in large buildings. In order to really benefit from submetering by evoking behavioral changes, and monitoring-based commissioning, it is critical for all circuits’ and plug loads’ data to be delivered to an energy information dashboard or building management system. This becomes more difficult with the PowerBlade, due to the limitations listed above. A comparison of the PTEM sensor presented in this chapter, the PowerBlade, and the Kill A Watt EZ meter is shown in Table 4.1.

	This work [27]	PowerBlade [26]	Kill A Watt EZ [21]
Size [l x w x t]	4.45" x 2.6" x $\frac{1}{16}$ "	1" x 1" x $\frac{1}{16}$ "	5.125" x 2.5" x 1.5"
Resolution	Noise floor: $\mu=14.4$ mA, $\sigma=1.8$ mA	2.2 W, $V_{line} = 120V_{RMS}$, PF=1	≈ 1 W
Accuracy	95% CI: 1.8% at 200 mA, 0.2% @ 2.7 A	95% CI: 9.5% @ 2.2W, 0.6% @ 1200W, PF=1, $V_{line} = 120V_{RMS}$	$> 0.2\%$
Power Dissipation	9.8 mA from 3.6V	180 mW	450 mW idle [26]; 10W @ $i_{load} = 10$ A
Bandwidth	Analog BW $> f_{Nyquist} = 960Hz$	$f_{Nyquist} = 1.26kHz$; analog BW not reported	
Data Interface	802.15.4 wireless	BLE wireless	Onboard display
Measured Wireless Range	$>40m$	20m	N/A
Cost per plug metered	Mfr: $< \$5$	Mfr: $\$10 - 15$	Purchase: $\$28$

Table 4.1: PTEM sensor comparison to state-of-the-art.

Chapter 5

Future Work

5.1 Tunneling Magnetoresistive Sensor for PASEM

	A1301 Hall sensor [33]	TMR2102 [34]	TMR2703 [34]	TMR2905 [34]
Sensitivity ¹	2.5 mV/G	24.5 mV/G	67.5 mV/G	250-300 mV/G
RMS Magnetic Noise ²	³ ≈19 mG	≈274 μG	≈274 μG	≈141 μG
Equivalent Noise Floor ⁴	380 mA _{RMS}	5.5 mA _{RMS}	5.5 mA _{RMS}	2.8 mA _{RMS}
Bias Current ⁵	10 mA	110 uA	83 uA	1 mA
Bandwidth	20 kHz	> 100 MHz	> 100 MHz	> 100 MHz
Package Size [l x w x t]	1.5x4x3mm SIP	3x3x0.75mm DFN8	3x3x0.75mm DFN8	3x3x0.75mm DFN8

Table 5.1: PASEM Hall effect sensor vs. TMR sensor comparison table.

In the PASEM circuit breaker metering system of Chapter 3, the accuracy of the power measurement is limited by the noise of the Hall effect sensor that is used to measure magnetic field and calculate the circuit's current. This noise can be reduced by averaging the signal over many cycles. However, performing this averaging introduces some difficulties in practice. Integrating over a long period of time, say one second, requires a precise frequency reference to drive the ADC's sampling clock without introducing phase shift that causes error in the

¹ $V_{DD} = 5\text{ V}$

²1st-order LPF, $f_p = 1\text{ kHz}$

³Assumes flat noise spectral density

⁴Breaker current equivalent, assuming 50 mG/Amp through breaker (thermal type). No averaging

⁵ $V_{DD} = 5\text{ V}$

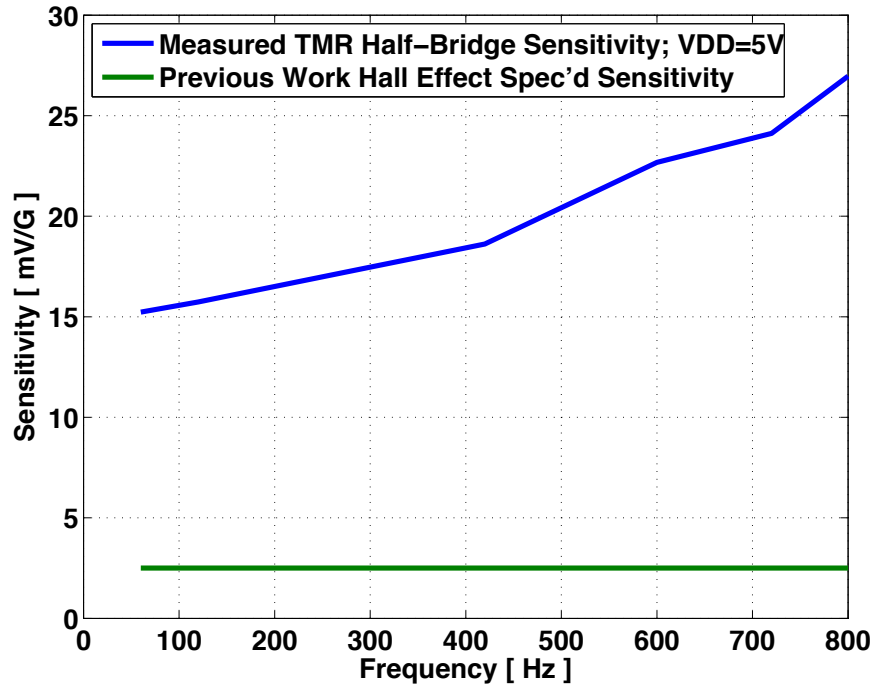


Figure 5.1: TMR sensor measured frequency response.

real power calculation (see Figure 3.9). A crystal oscillator frequency reference can be added to the sensor to serve this purpose, but can still only be used for 64-128x cycle averaging.

Tunneling magnetoresistive (TMR) sensors are based on quantum mechanical tunneling, are typically used in hard disk drive read heads, and have properties that are far superior to the Hall effect sensors used in the aforementioned PASEM work; see Table 5.1. The magnetic sensitivity of TMR sensors can be >100x higher, leading to relaxed requirements in subsequent amplifiers. At the same time, the noise levels are >100x lower than the Hall sensor used in this work, which substantially improves the current measurement resolution without any averaging. With much improved signal and noise characteristics, the power dissipation of the TMR sensors can also be two orders of magnitude lower than Hall sensors.

Therefore, a TMR sensor could be used to make a much lower power, more accurate circuit breaker power sensor based on the concepts presented in this dissertation. By integrating a TMR sensor in a new PASEM design and duty-cycling the microcontroller and analog amplifiers, the PASEM board's total current consumption could feasibly be reduced to about 250 μA . As an initial step towards this goal, the sensitivity of a prototype TMR sensor was measured in a Helmholtz coil. The measured sensitivity at various frequencies can be seen in Figure 5.1 in comparison to the A1301 Hall effect sensor. It is believed that the variation in sensitivity with frequency is due to non-idealities in the test setup.

5.2 Single-Chip Vector Sensing Breaker Meter

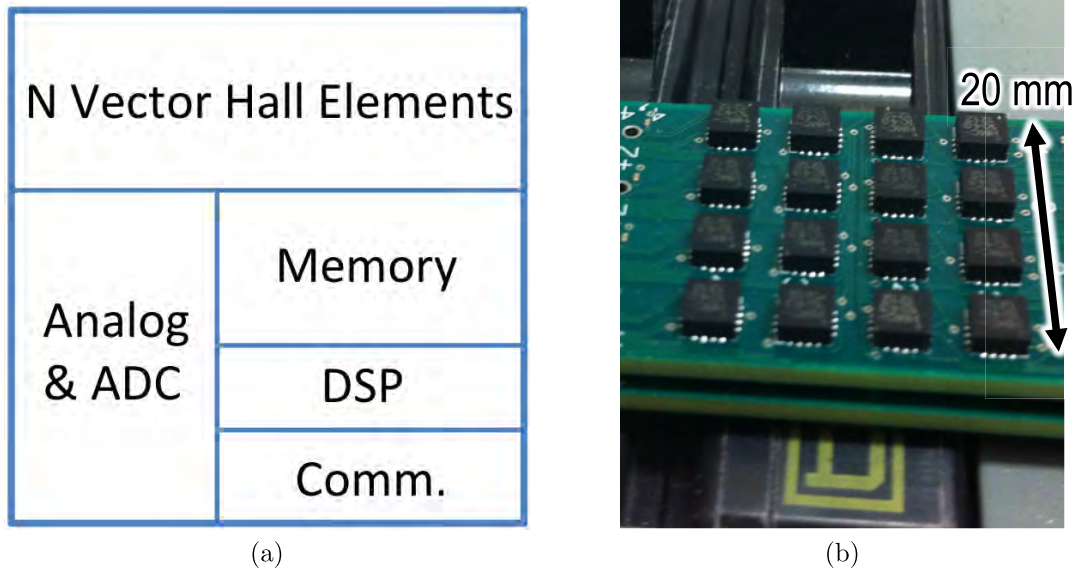


Figure 5.2: (a) Single-chip vector magnetic field sensing power meter block diagram. (b) PCB prototype sensor with 4x4x2 array of 3-axis magnetic field sensors.

Again considering Figure 3.12, it can be seen that the magnetic field vectors incident on the PASEM sensor have different orientations depending on the source of the field. With one single-axis magnetic field sensor per PASEM, the information captured about the fields makes this differentiation difficult. However, if many vector magnetic field sensors are integrated in a PASEM sensor, a much more detailed picture of the magnetic fields can be obtained. With more information about the fields, and, thus, the currents, more effective crosstalk mitigation should be possible.

A photo of a prototype vector magnetic field sensor PCB designed and tested is shown in Figure 5.2b. This sensor has a 4x4x2 array of analog 3-axis anisotropic magnetoresistive (AMR) magnetic field sensors. An example measurement taken with the vector sensor on a circuit breaker with a solenoid inside is shown in Figure 5.3. As expected due to the solenoid, the measured magnetic field takes on the characteristic shape of a magnetic dipole. A few of the sensors are not working properly, due to difficulties realigning the magnetic domains of the AMR sensors. It is easy to imagine that having real-time measured data like this could drive the development of a plethora of new intelligent algorithms for power sensing.

Figure 5.2a is a block diagram of the single-chip vector magnetic field sensing power meter. A number of vector Hall sensor elements [35]–[38] would be integrated on the same substrate

as the other CMOS circuits. The analog and mixed-signal circuits could be power-optimized for the specific bandwidth and dynamic range required in this application. Digital signal processing hardware would also be included for efficient computation of crosstalk cancellation algorithms and AC power calculations. Integrating all of these application-specific circuits into one chip could decrease the cost of a circuit breaker power meter by roughly another 5-10x, making panel submetering installation a total no-brainer for building owners. From very conservative estimates⁶ extrapolated from reported submetering installation costs and energy savings in [5], a low-cost single-chip meter could easily enable installation payback periods of <2 weeks in commercial buildings. While similar data is not available for real-world residential installations, an average payback period of ≈ 8 months⁷ is likely attainable with \$50/panel installed submetering costs [2].

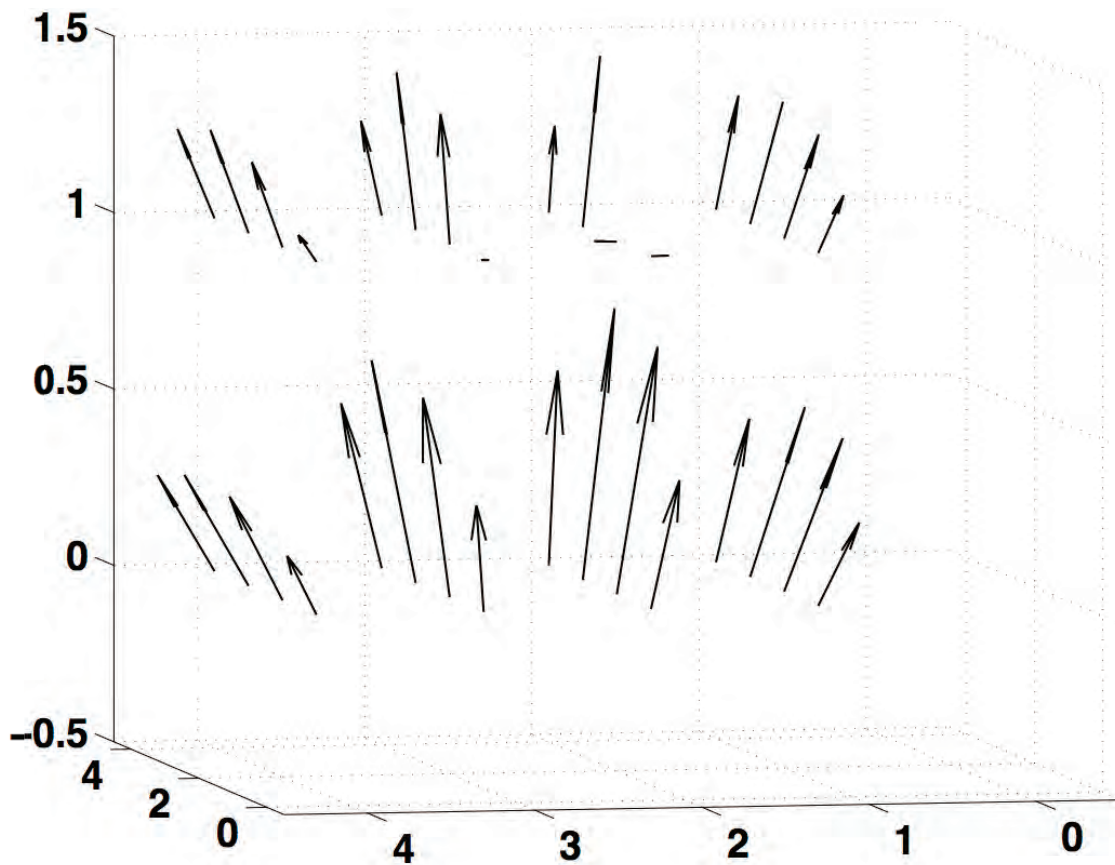


Figure 5.3: Measured magnetic field with 4x4x2 vector sensor array on solenoidal circuit breaker.

⁶5% energy consumption reduction in buildings with pre-existing high efficiency ratings. A factor of 50 reduction in first year submetering project costs compared to today's commercial submetering solutions.

⁷5% energy consumption reduction in an average residential building with one panel.

Chapter 6

Conclusions

Immense efforts need to be made by the human race to reduce the harm being done to the earth by the emission of greenhouse gases. People need to be more aware of their energy usage, and realize that the majority of this can be traced back to sources that are harmful to the environment. While reducing GHG emissions associated with the transportation sector has been very much in the public eye, not nearly as many people are aware of the substantial contribution that electricity usage is making to global warming. While building studies are lacking in some areas due to drawbacks associated with traditional technologies, submetering has been shown to enable 5-30% reductions in electrical energy consumption in many building types through monitoring-based commissioning and occupant behavioral changes.

In Chapter 3, a new sensor system has been presented for building submetering at the circuit breaker panel that solves many issues inhibiting the widespread adoption of current technologies. The measurements in this paper have shown that our sensor accurately measures real power with a 960 Hz usable bandwidth, and it works well in a residential installation with various types of loads. Our submetering solution includes cost effective hardware that is suitable for installation without an electrician, and is easy to produce without an exotic manufacturing process. The installed cost of our system is estimated to be \$250 per panel - $\approx 10x$ lower than other available solutions - with installation time also decreased substantially. Future work was presented that could further decrease the system's installed cost by another 5-10x.

In Chapter 4, the design and characterization of a low-cost, *plug-through* energy monitor for electrical submetering of plug load devices in buildings was discussed. The sensor uses an inductive current sensor printed into the PCB to measure current non-intrusively. This enables a form factor that is $\approx 10x$ thinner than traditional plug meters, and allows the device to be hidden out of sight behind an outlet faceplate. Inductive current sensing also allows the meter itself to be very low power, consuming only 35 mW for power sensing and 802.15.4 wireless communication. Voltage and current signals are sampled at 1920 Hz for handling non-linear loads, and the measured noise floor is approximately 2.4W with 120 V RMS mains. The PTEM sensor can be fabricated using a standard 2-layer PCB process and

its BOM cost is only \approx \$5. The sensor was tested in a real world deployment and it is able to effectively measure time-varying loads with non-unity power factors.

In this dissertation, effective and practical sensor systems with the potential to enable pervasive building electrical submetering at plugs and panels have been presented. Increasing the energy efficiency of buildings needs to become a widespread effort, and this should be supported by new government regulations and incentives. If all buildings in the United States were to improve their energy efficiency by only 10%, this would reduce greenhouse gas emissions by an amount equivalent to approximately 2 *trillion* miles driven in a 30 mpg car, every year [39], [40]. Hopefully the novel technologies developed by this research work can be true catalysts in these future efforts.

Bibliography

- [1] U. S. EPA, *Inventory of U.S. greenhouse gas emissions and sinks, 1990-2013*. 2015. [Online]. Available: www.epa.gov/climatechange/ghgemissions/usinventoryreport.html.
- [2] Energy Information Agency, *Annual Energy Outlook 2015*. [Online]. Available: www.eia.gov/forecasts/aeo/er/.
- [3] *PG&E SmartMeter product website*. [Online]. Available: <http://pge.com/en/myhome/customerservice/smartmeter/index.page>.
- [4] National Science and Technology Council Committee on Technology, Subcommittee on Buildings Technology Research and Development, *Submetering of Building Energy and Water Usage*. 2011.
- [5] P. Henderson and M. Waltner, “Real-time energy management,” Natural Resources Defense Council, 2013.
- [6] N. R. E. Laboratory, *Plug Load Behavioral Change Demonstration Project*. 2011. [Online]. Available: <http://www.nrel.gov/docs/fy11osti/52248.pdf>.
- [7] S. Darby *et al.*, “The effectiveness of feedback on energy consumption,” *A Review for DEFRA of the Literature on Metering, Billing and direct Displays*, vol. 486, p. 2006, 2006.
- [8] A. Faruqui, S. Sergici, and A. Sharif, “The impact of informational feedback on energy consumption—A survey of the experimental evidence,” *Energy*, vol. 35, no. 4, pp. 1598–1608, 2010.
- [9] W. Abrahamse, L. Steg, C. Vlek, and T. Rothengatter, “A review of intervention studies aimed at household energy conservation,” *Journal of environmental psychology*, vol. 25, no. 3, pp. 273–291, 2005.
- [10] New York State Energy Research and Development Authority, *Residential Electrical Submetering Manual*. Oct. 1997.
- [11] E. Mills, “Monitoring based commissioning: benchmarking analysis of 24 uc/csu/iou projects,” *Lawrence Berkeley National Laboratory*, 2009.

- [12] G. Sullivan, W. Hunt, R. Pugh, W. Sandusky, T. Koehler, and B. Boyd, “Metering best practices: a guide to achieving utility resource efficiency, release 2.0,” Department of Energy Federal Energy Management Program, 2011.
- [13] E. Star, “Sub-metering energy use in colleges and universities: incentives and challenges,” *Energy Star*. https://www.energystar.gov/ia/business/higher_ed/Submeter_energy_use.pdf. (Accessed August, 2011), 2002.
- [14] Q. Xu, I. Paprotny, R. White, and P. Wright, “Energy submetering for circuit breaker panels using mems or mesoscale passive proximity current sensor,” in *PowerMEMS 2010*, 2010.
- [15] Q. Xu, M. Seidel, I. Paprotny, R. White, and P. Wright, “Integrated centralized electric current monitoring system using wirelessly enabled non-intrusive ac current sensors,” in *Sensors, 2011 IEEE*, 2011, pp. 1998–2001. DOI: 10.1109/ICSENS.2011.6127284.
- [16] R. Send, Q. Xu, I. Paprotny, R. White, and P. Wright, “Granular radio energy-sensing node (green): a 0.56 cm³ wireless stick-on node for non-intrusive energy monitoring,” in *Sensors, 2013 IEEE*, Nov. 2013, pp. 1–4. DOI: 10.1109/ICSENS.2013.6688133.
- [17] Q. Xu, I. Paprotny, M. Seidel, R. White, and P. Wright, “Stick-on piezoelectromagnetic ac current monitoring of circuit breaker panels,” *Sensors Journal, IEEE*, vol. 13, no. 3, pp. 1055–1064, Mar. 2013, ISSN: 1530-437X. DOI: 10.1109/JSEN.2012.2234738.
- [18] S. N. Patel, S. Gupta, and M. S. Reynolds, “The design and evaluation of an end-user-deployable, whole house, contactless power consumption sensor,” in *Proceedings of the SIGCHI Conference on Human Factors in Computing Systems*, ser. CHI ’10, Atlanta, Georgia, USA: ACM, 2010, pp. 2471–2480, ISBN: 978-1-60558-929-9. DOI: 10.1145/1753326.1753700. [Online]. Available: <http://doi.acm.org/10.1145/1753326.1753700>.
- [19] M. Lorek, F. Chraim, K. Pister, and S. Lanzisera, “COTS-based stick-on electricity meters for building submetering,” in *SENSORS, 2013 IEEE*, Nov. 2013, pp. 1–4. DOI: 10.1109/ICSENS.2013.6688592.
- [20] —, “COTS-based stick-on electricity meters for building submetering,” *Sensors Journal, IEEE*, vol. 14, no. 10, pp. 3482–3489, Oct. 2014, ISSN: 1530-437X. DOI: 10.1109/JSEN.2014.2346765.
- [21] *Kill A Watt EZ product website*. [Online]. Available: <http://www.p3international.com/products/p4460.html>.
- [22] *SmartPower Outlet product website*. [Online]. Available: <https://shop.smartthings.com/#!/products/smartpower-outlet>.
- [23] [Online]. Available: <http://www.slocounty.ca.gov/planning/Energy/KM.htm>.
- [24] [Online]. Available: <http://9to5toys.com/2015/01/03/smartthings-home-automation-review/>.

- [25] Y. Kim, T. Schmid, Z. M. Charbiwala, and M. B. Srivastava, “Viridiscope: design and implementation of a fine grained power monitoring system for homes,” in *Proc. Ubicomp09*, 2009, pp. 245–254.
- [26] S. DeBruin, B. Ghena, Y.-S. Kuo, and P. Dutta, “Powerblade: a low-profile, true-power, plug-through energy meter,” in *Proceedings of the 13th ACM Conference on Embedded Networked Sensor Systems*, ACM, 2015, pp. 17–29.
- [27] M. Lorek, F. Chraim, and K. Pister, “Plug-through energy monitor for plug load electrical devices,” in *SENSORS, 2015 IEEE*, Nov. 2015, pp. 1–4.
- [28] Wikipedia, *555 california street — wikipedia, the free encyclopedia*, [Online; accessed 1-December-2015], 2015. [Online]. Available: https://en.wikipedia.org/w/index.php?title=555_California_Street&oldid=689428510.
- [29] *New York State Energy Research and Development Authority website*. [Online]. Available: <http://www.nyserda.ny.gov/All-Programs/Programs/Submetering-for-Master-Metered-Buildings>.
- [30] S. Dawson-Haggerty, X. Jiang, G. Tolle, J. Ortiz, and D. Culler, “sMAP: a simple measurement and actuation profile for physical information,” in *Proceedings of the 8th ACM Conference on Embedded Networked Sensor Systems*, ser. SenSys ’10, Switzerland: ACM, 2010, pp. 197–210, ISBN: 978-1-4503-0344-6. DOI: 10.1145/1869983.1870003.
- [31] *Watts Up Pro product website*. [Online]. Available: <http://www.wattsupmeters.com/secure/products.php?pn=0>.
- [32] T. Watteyne, X. Vilajosana, B. Kerkez, F. Chraim, K. Weekly, Q. Wang, S. Glaser, and K. Pister, “Openwsn: a standards-based low-power wireless development environment,” *Transactions on Emerging Telecommunications Technologies*, vol. 23, no. 5, pp. 480–493, 2012.
- [33] *Allegro A1301/2 datasheet*. [Online]. Available: <http://www.allegromicro.com/~media/Files/Datasheets/A1301-2-Datasheet.ashx?la=en>.
- [34] *MultiDimension Technology TMR sensors*. [Online]. Available: http://www.dowaytech.com/en/sensor/linear_sensors.html.
- [35] C. Schott, J.-M. Waser, and R. Popovic, “Single-chip 3-d silicon hall sensor,” *Sensors and Actuators A: Physical*, vol. 82, no. 1, pp. 167–173, 2000.
- [36] F. Burger, P.-A. Besse, and R. Popovic, “New fully integrated 3-d silicon hall sensor for precise angular-position measurements,” *Sensors and Actuators A: Physical*, vol. 67, no. 1, pp. 72–76, 1998.
- [37] P. Kejik, E. Schurig, F. Bergsma, and R. Popovic, “First fully cmos-integrated 3d hall probe,” in *Solid-State Sensors, Actuators and Microsystems, 2005. Digest of Technical Papers. TRANSDUCERS’05. The 13th International Conference on*, IEEE, vol. 1, 2005, pp. 317–320.

- [38] M. Paranjape, I. Filanovsky, and L. Ristic, “A 3-d vertical hall magnetic-field sensor in cmos technology,” *Sensors and Actuators A: Physical*, vol. 34, no. 1, pp. 9–14, 1992.
- [39] J. Alson, A. Hula, A. Bunker, *et al.*, “Light-duty automotive technology, carbon dioxide emissions, and fuel economy trends: 1975 through 2013,” *Appendix F, US Environmental Protection Agency, Ann Arbor, Michigan, available at: <http://www.epa.gov/oms/fetrends.htm#report>*, 2014.
- [40] *NRDC well-to-wheels alternative fuels comparison chart*. [Online]. Available: <https://www.e2.org/ext/doc/NRDC%20Well-to-Wheels%20Alt%20Fuels%20Rainbow%20Chart.pdf>.